

# A CONSERVATIVE, POSITIVITY PRESERVING SCHEME FOR REACTIVE SOLUTE TRANSPORT PROBLEMS IN MOVING DOMAINS

SIBUSISO MABUZA, DMITRI KUZMIN, SUNČICA ČANIĆ, AND MARTINA BUKAČ

**ABSTRACT.** We study the mathematical models and numerical schemes for reactive transport of a soluble substance in deformable media. The medium is a channel with compliant adsorbing walls. The solutes are dissolved in the fluid flowing through the channel. The fluid, which carries the solutes, is viscous and incompressible. The reactive process is described as a general physico-chemical process taking place on the compliant channel wall. The problem is modeled by a convection-diffusion adsorption-desorption equation in moving domains. We present a conservative, positivity preserving, high resolution ALE-FCT scheme for this problem in the presence of dominant transport processes and wall reactions on the moving wall. A Patankar type time discretization is presented, which provides conservative treatment of nonlinear reactive terms. We establish CFL-type constraints on the time step, and show the mass conservation of the time discretization scheme. Numerical simulations are performed to show validity of the schemes against effective models under various scenarios including linear adsorption-desorption, irreversible wall reaction, infinite adsorption kinetics, and nonlinear Langmuir kinetics. The grid convergence of the numerical scheme is studied for the case of fixed meshes and moving meshes in fixed domains. Finally, we simulate reactive transport in moving domains under linear and nonlinear chemical reactions at the wall, and show that the motion of the compliant channel wall enhances adsorption of the solute from the fluid to the channel wall. Consequences of this result are significant in the area of, e.g., nano-particle cancer drug delivery. Our result shows that periodic excitation of the cancerous tissue using, e.g., ultrasound, may enhance adsorption of cancer drugs carried by nano-particles via the human vasculature.

**Key words.** Reactive Transport, Flux Corrected Transport, Arbitrary Lagrangian-Eulerian Methods, Convection Dominated Flow

## 1. INTRODUCTION

The reactive transport of chemical solutes in deformable media is an important problem with wide-spread engineering and biological applications. These applications include the transport of dissolved solutes in blood vessels [63], chemical transport in reactors, chromatographic separation [1, 8, 54, 60], and the transport of solutes in petroleum recovery [34]. Reactive transport is usually studied under three different flow regimes, which are *diffusion dominated flow*, *convection dominated flow*, and *chaotic advection* [1, 60]. For the first flow regime, diffusion is more influential than convection in the overall flow of the solutes. In the second regime, the convection is more influential than diffusion, giving rise to the so called Taylor dispersion effects. An example of this is Taylor dispersion-mediated mixing [1]. In the third flow regime, turbulent mixing is observed. In this paper we concern ourselves with flow characterized by dominant convection, typically associated with Taylor dispersion. This is the case mathematically defined by moderate to large Péclet numbers  $Pe \gg 1$ .

Our study concerns chemical solutes that are dissolved in a viscous incompressible fluid flowing in a channel with moving walls. The fluid flow is modeled by the Navier-Stokes equations. The location of the moving boundary is calculated using a fluid-structure interaction (FSI) solver, previously developed in [14, 33]. For the problem studied in this manuscript, the location of the moving boundary and the fluid flow are given, and are obtained using a FSI solver. For more details on mathematical models, analysis and numerical schemes for incompressible fluid flow in compliant domains please see [14, 15, 19–23, 33, 37, 52], and the references therein.

The solute species are assumed to have no effect on the flow character of the fluid, and can thus be treated as trace particles. Solute dynamics in the bulk fluid are described by a convection-diffusion equation in a moving

domain with the convection flux defined by the (given) fluid velocity. The reactive process is described as a general physico-chemical process taking place on the compliant channel wall. The reaction process may consist of adsorption-desorption, multi-stage reactions, or catalysed wall reactions. Common examples of such physico-chemical models are the linear Henry’s law, Langmuir adsorption, Freundlich adsorption, Langmuir-Freundlich adsorption and Langmuir-Hinshelwood catalytic reactions among many others [35,61]. Our model extends the reactive transport models for various reaction systems in a fixed cylindrical channel, studied in [8, 24–26, 47–49, 51, 60], to the reactive transport models in channels with moving walls. More complex fixed channel geometries are considered in [12, 53]. Notable examples of reactive transport with moving domains can be found in [31, 38]. In [38], the reactive process affects the wall deformation by precipitation and dissolution of solutes on the wall. This leads to a coupled fluid flow and solute transport problem in which the fluid profile and wall deformation is constantly updated. In [31], erosion of a solid domain resembling a stent embedded in arterial wall is considered. The solute transport problem involves the reaction of drug solutes on the boundary of the stent.

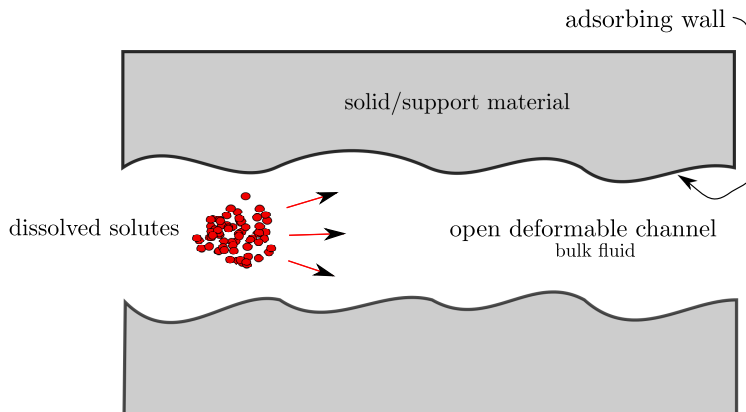


**Figure 1.** Reactive transport phenomena in a narrow deformable channel with active adsorbing walls. The chemical solutes are dissolved in a solvent flowing under a pressure gradient, and undergoing (Taylor) dispersion in the cylindrical channel. Upon reaching the channel walls they are adsorbed due to their affinity to the wall. The solid/supporting material has zero porosity. Compliance of the wall is due to the normal stress exerted by the fluid onto the compliant channel wall.

For Taylor dispersion and for other convection dominated flows, numerical schemes for solute transport may lead to undesirable numerical artefacts. These are usually shown by oscillations in the profile of the numerical solution (solute concentration). Therefore, such schemes require stabilization to deal with oscillations that occur in the numerical solution. In the finite element context, stabilization methods of FCT type were studied by Löhner et al. in [44, 45]. Recently there have been studies for various **fixed domain problems** in [40–42, 50] and [36]. In [36], a comparative study of various stabilization schemes, including FCT was done. The FCT type of schemes emerges as the most superior and efficient. In moving domains, upwinding has been applied to convection-diffusion problems by Badia et al. in [6], and Boiarkine et al. in [11]. In both of those papers the finite element discretization in arbitrary Lagrangian-Eulerian (ALE) framework is used. The work of Badia et al. uses the orthogonal subgrid scale type stabilization, while the work of Boiarkine et al. constructs an FCT type of stabilization. In this paper, we extend the FCT type design under the ALE framework to general reactive transport problems. Additionally, we introduce a linearization technique for treating nonlinear reaction terms in a conservative way following the Patankar linearization techniques, proposed in [16–18] and [32]. This linearization is designed such that second order time discretization is achieved, and the fully discrete scheme is mass conservative. Furthermore, our second-order time discretization will ensure that the geometric conservation law (GCL) is satisfied.

To validate the numerical scheme, we consider first the transport in fixed channels with fixed and moving meshes. The tests include reactive processes such as irreversible reactions, linear adsorption-desorption, infinite adsorption, and nonlinear adsorption processes. The numerical results of our scheme are compared to the solutions of effective models considered in [25, 27, 60], showing excellent agreement.

We then consider grid convergence on fixed and moving meshes for the scheme under the linear and nonlinear chemical reactions, mentioned above. The moving mesh error is studied to show that the solution is “mesh independent” up to a certain tolerance, showing excellent mesh independence property.

We conclude this manuscript by simulating reactive solute transport in moving domains for both linear Henry’s law, and nonlinear Langmuir adsorption. We show that the motion of the channel walls enhances solute adsorption to the channel wall. Consequences of this result are significant in the area of, e.g., nano-particle cancer treatment. Our result shows that the excitation of the cancerous tissue using, e.g., ultrasound, may enhance adsorption of cancer drugs carried by nano-particles via the human vasculature.

## 2. MATHEMATICAL FORMULATION

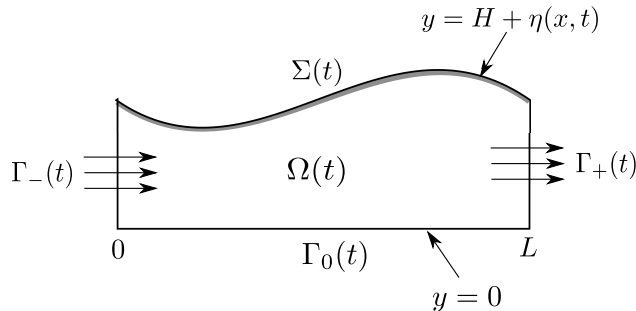


**Figure 2.** The schematic of the compliant channel with an active deformable wall  $\Sigma(t)$ .

We present a model for a single solute species transported in a compliant 2D channel

$$\Omega(t) = \{\mathbf{x} = (x, y) : x \in (0, L), y \in (0, H + \eta(x, t))\}.$$

The function  $\eta$  defines the radial movement of the channel wall. For simplicity, only the upper wall deformation will be considered. The solute is convected by a fluid with a (given) velocity field  $\mathbf{v}$ . The dissolved solutes undergo non-equilibrium physico-chemical processes on the compliant wall  $\Sigma(t) = \{\mathbf{x} = (x, y) : x \in (0, L), y = H + \eta(x, t)\}$ . The main equation defined on  $\Omega(t)$ , is given by the convection-diffusion equation. This is coupled with a flux equation on  $\Sigma(t)$ , which describes the transfer of the solutes from the bulk fluid to the wall.

To formulate the problem in the moving domain  $\Omega(t)$ , we make use of the ALE mapping approach, as presented in [11, 29, 52] and [30]. Consider the time dependent domain, given by  $\Omega(t)$ , the reference domain, given by  $\hat{\Omega}$ , and let  $\{\mathcal{A}_t\}$  be a family of maps from  $\hat{\Omega}$  onto  $\Omega(t)$ , called the ALE maps, such that

$$\mathcal{A}_t : \hat{\Omega} \rightarrow \Omega(t), \quad \mathbf{x}(\hat{\mathbf{x}}, t) = \mathcal{A}_t(\hat{\mathbf{x}}),$$

is a diffeomorphic function for each  $t \in [0, T]$ . The coordinate  $\mathbf{x} \in \Omega(t)$  is called the Eulerian coordinate, and  $\hat{\mathbf{x}} \in \hat{\Omega}$  is the ALE coordinate. In the same spirit, we define ALE counterparts of functions defined on  $\Omega(t)$ . Let  $f : \Omega(t) \times [0, T] \rightarrow \mathbb{R}$  be an arbitrary function, then we can write  $\hat{f} = f \circ \mathcal{A}_t$  such that  $\hat{f} : \hat{\Omega} \times [0, T] \rightarrow \mathbb{R}$  satisfies  $f(\mathbf{x}, t) = \hat{f}(\hat{\mathbf{x}}, t)$ , for  $\mathbf{x} \in \mathcal{A}_t(\hat{\mathbf{x}})$ . We can also study time derivatives in the Eulerian frame and present their counterparts in the ALE frame as  $\frac{\partial f}{\partial t}\Big|_{\mathbf{x}}(\mathbf{x}, t) = \frac{\partial \hat{f}}{\partial t}\Big|_{\hat{\mathbf{x}}}(\hat{\mathbf{x}}, t)$ . The domain velocity, which was already mentioned before when discussing boundary conditions, is given by

$$\mathbf{w}(\mathbf{x}, t) = \frac{\partial \mathbf{x}}{\partial t}\Big|_{\hat{\mathbf{x}}}(\hat{\mathbf{x}}, t).$$

The Eulerian time-derivative can be cast in ALE framework by using the chain rule as  $\frac{\partial f}{\partial t}\Big|_{\hat{\mathbf{x}}} = \frac{\partial f}{\partial t}\Big|_{\mathbf{x}} + \mathbf{w} \cdot \nabla f$ , which implies that  $\frac{\partial f}{\partial t}\Big|_{\mathbf{x}} = \frac{\partial f}{\partial t}\Big|_{\hat{\mathbf{x}}} - \mathbf{w} \cdot \nabla f$ . This will allow us to reformulate our time dependent problem in the ALE framework. The problem in the ALE framework can then be written in non-conservative and

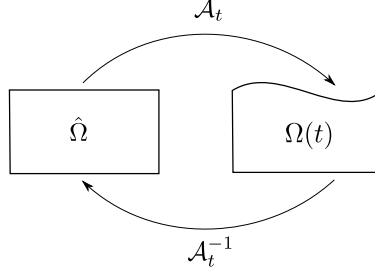


**Figure 3.** The ALE map from fixed  $\hat{\Omega}$  to moving  $\Omega(t)$ .

conservative form. For the purposes of writing the problem in conservative ALE form, we will need the Jacobian of the ALE map  $\mathcal{A}_t$ , defined by  $\mathbf{J}_{\mathcal{A}_t} = \frac{\partial \mathbf{x}}{\partial \hat{\mathbf{x}}}$ , and its determinant  $\mathcal{J}_{\mathcal{A}_t} = \det(\mathbf{J}_{\mathcal{A}_t})$ , from which we can relate the Jacobian determinant to its derivative by the Euler expansion formula as  $\frac{\partial \mathcal{J}_{\mathcal{A}_t}}{\partial t} \Big|_{\hat{\mathbf{x}}} = \mathcal{J}_{\mathcal{A}_t} \nabla \cdot \mathbf{w}$  [4].

With the above description of the ALE formulation, we can now summarize the main model. Let the solute concentration in the bulk fluid be denoted by  $c^f$ . Let the (adsorbed) solute concentration, which is the mass per unit length on the compliant channel wall, be denoted by  $c^w$ . The reactive transport model for the solute dynamics in the deformable channel is therefore given by the following:

$$(1) \quad \left\{ \begin{array}{l} \frac{\partial c^f}{\partial t} + \nabla \cdot (\mathbf{v}c^f - D\nabla c^f) = 0, \text{ in } \Omega(t), t \in (0, T], \\ (\tilde{\mathbf{v}}c^f - D\nabla c^f) \cdot \mathbf{n} = \mathcal{J}_{\mathcal{A}_t}^{-1} \frac{D(\mathcal{J}_{\mathcal{A}_t}c^w)}{Dt} = k_d(\Lambda(c^f) - c^w) \text{ on } \Sigma(t), t \in (0, T], \\ (\tilde{\mathbf{v}}c^f - D\nabla c^f) \cdot \mathbf{n} = (\mathbf{v}c_{in}) \cdot \mathbf{n} \text{ on } \Gamma_-(t), t \in (0, T], \\ (\tilde{\mathbf{v}}c^f - D\nabla c^f) \cdot \mathbf{n} = 0, \text{ on } \Gamma_0(t), t \in (0, T], \\ -D\nabla c^f \cdot \mathbf{n} = 0, \text{ on } \Gamma_+(t), t \in (0, T], \\ c^f|_{t=0} = c_0^f \text{ in } \hat{\Omega}, c^w|_{t=0} = c_0^w \text{ on } \hat{\Sigma}. \end{array} \right.$$

Here,  $\tilde{\mathbf{v}}$  is the relative fluid velocity, which is defined by  $\tilde{\mathbf{v}} = \mathbf{v} - \mathbf{w}$ . The domain at  $t = 0$  is given by  $\hat{\Omega} = \Omega(0)$ , with  $\hat{\Sigma} = \Sigma(0)$ . The general nonlinear wall adsorption-desorption is described by the isotherm  $\Lambda$ . The isotherm is taken to be Lipschitz continuous as a function in  $\mathbb{R}_+$ , and continuous as a function in  $\mathbb{R}$ .

**Remark 2.1.** For general non-Lipschitz isotherms, the problem can be solved using Lipschitz regularization. For more details, see [9, 55] for the case of fixed domains.

**Remark 2.2.** For the study of linear transport such as Henry's law (linear adsorption-desorption), and for irreversible wall reaction, the isotherm  $\Lambda$  is a linear function. For infinite adsorption, the rate  $k_d$  is infinite, and this requires a different description of the flux function on  $\Sigma(t)$ . This will be discussed in detail under numerical results in section 5.

**2.1. The fluid velocity and motion of the fluid domain.** The fluid velocity and the motion of the fluid domain are obtained as a solution of a fluid-structure interaction problem. This calculation is completely decoupled from the reactive transport problem. The fluid is modeled by the incompressible Navier-Stokes equations, while the elastodynamics of the lateral boundary by the cylindrical linearly viscoelastic Koiter shell equations. The velocity of the fluid is denoted by  $\mathbf{v}$ , while the wall deformation is given by  $\eta$ . The wall deformation is **only radial**, which in 2D corresponds to vertical movement in the  $y$ -direction. At the endpoints, the wall is fixed. The problem can then be summarized by

$$(2) \quad \left\{ \begin{array}{l} \rho_f \left( \frac{\partial \mathbf{v}}{\partial t} + \mathbf{v} \cdot \nabla \mathbf{v} \right) = \nabla \cdot \boldsymbol{\sigma}, \quad \nabla \cdot \mathbf{v} = 0 \text{ in } \Omega(t), \quad t \in (0, T), \\ \text{where } \boldsymbol{\sigma} = -p\mathbf{I} + 2\mu\mathbf{D}(\mathbf{v}), \quad \mathbf{D}(\mathbf{v}) = \frac{1}{2}(\nabla \mathbf{v} + (\nabla \mathbf{v})^T), \\ \boldsymbol{\sigma} \mathbf{n}(0, y, t) = -\bar{p}(t)\mathbf{n}, \quad \boldsymbol{\sigma} \mathbf{n}(L, y, t) = \mathbf{0}, \text{ on } (0, H) \times (0, T), \\ \frac{\partial v_1}{\partial y}(x, 0, t) = 0, \quad v_2(x, 0, t) = 0, \text{ on } (0, L) \times (0, T), \\ \rho_s h_s \frac{\partial^2 \eta}{\partial t^2} + C_0 \eta - C_1 \frac{\partial^2 \eta}{\partial x^2} + D_0 \frac{\partial \eta}{\partial t} - D_1 \frac{\partial^3 \eta}{\partial t \partial x^2} = f_2, \text{ on } (0, L) \times (0, T) \\ \text{where } f_2 = -\sqrt{1 + \left( \frac{\partial \eta}{\partial x} \right)^2} \boldsymbol{\sigma} \mathbf{n} \cdot \mathbf{e}_2, \quad \mathbf{e}_2 = (0, 1), \text{ on } \Sigma(t), \\ v_1 = 0, \quad v_2 = \frac{\partial \eta}{\partial t}, \text{ on } \Sigma(t), \quad t \in (0, T) \\ \mathbf{v}(\mathbf{x}, 0) = \mathbf{0}, \text{ in } \hat{\Omega}, \quad \eta(x, 0) = \frac{\partial \eta}{\partial t} = 0, \text{ for } x \in (0, L), \\ \eta(0, t) = \eta(L, t) = 0, \quad t \in (0, T). \end{array} \right.$$

Here,  $\rho_f$  is the fluid density,  $\rho_s$  is the wall density,  $h_s$  is the elastic wall thickness,  $C_0$  and  $C_1$  are the elastic constants, and  $D_0$  and  $D_1$  are the viscoelastic constants,  $f_2$  is the radial projection of the force applied to the structure, and  $\mu$  is the fluid viscosity.

Notice that at the bottom boundary where  $y = 0$ , symmetry boundary condition is assumed. This boundary is denoted by  $\Gamma_0$  in Figure 2. Furthermore, on the inlet and outlet boundaries, we have a normal stress boundary condition which occurs naturally with the weak formulation. This is a common choice of boundary conditions in blood flow modeling [7, 14].

For the purposes of this paper we prescribe the normal stress data such that the left boundary i.e.,  $x = 0$ , correspond to the physical inlet:

$$\Gamma_-(t) := \{\mathbf{x} : \mathbf{v} \cdot \mathbf{n} < 0\},$$

while the right boundary,  $x = L$ , corresponds to the physical outlet:

$$\Gamma_+(t) := \{\mathbf{x} : \mathbf{v} \cdot \mathbf{n} > 0\}.$$

The numerical solution of this problem was obtained using a loosely coupled fluid-structure interaction scheme, first introduced in [33], and rigorously analysed in [20].

### 3. VARIATIONAL FORMULATION

We begin this section by introducing a space of test functions defined on the reference domain  $\hat{\Omega}$ . It will be sufficient to consider the test functions belonging to the space  $H^1(\hat{\Omega})$ . The functions in this space are time independent. With the help of the ALE mapping, we construct the test space  $\mathbf{W}(t)$ , on the moving domain  $\Omega(t)$ , as follows

$$\mathbf{W}(t) := \{\psi : \Omega(t) \rightarrow \mathbb{R} : \psi = \hat{\psi} \circ \mathcal{A}_t^{-1}, \quad \hat{\psi} \in H^1(\hat{\Omega})\}.$$

This defines a time dependent test space on the moving domain  $\Omega(t)$ . We also choose the test space for functions on the wall to be  $L^2(\hat{\Sigma})$ , and similarly construct the moving wall test space as follows

$$\mathbf{Y}(t) = \{\varphi : \Sigma(t) \rightarrow \mathbb{R} : \varphi = \hat{\varphi} \circ \mathcal{A}_t^{-1}, \quad \hat{\varphi} \in L^2(\hat{\Sigma})\}.$$

From [52] and [29] we know that there is an isomorphic relation between the fixed and moving domains under the ALE map, provided  $\mathcal{A}_t \in \mathbf{W}^{1,\infty}(\hat{\Omega})$ , and  $\mathcal{A}_t^{-1} \in \mathbf{W}^{1,\infty}(\Omega(t))$ . This gives an isomorphism between the test functions in the moving domain, and those in the fixed reference domain.

To get the conservative form, we test by  $\varphi \in \mathbf{W}(t)$ , the following form of the convection-diffusion equation whose time derivative is in the fixed reference domain:

$$(3) \quad \frac{1}{\mathcal{J}_{\mathcal{A}_t}} \frac{\partial(\mathcal{J}_{\mathcal{A}_t} c^f)}{\partial t} \Big|_{\hat{\mathbf{x}}} + \nabla \cdot ((\mathbf{v} - \mathbf{w})c^f - D\nabla c^f) = 0, \text{ in } \Omega(t).$$

As a result, we get the following

$$(4) \quad \int_{\Omega(t)} \varphi \frac{1}{\mathcal{J}_{\mathcal{A}_t}} \frac{\partial}{\partial t} (\mathcal{J}_{\mathcal{A}_t} c^f) \Big|_{\hat{\mathbf{x}}} d\mathbf{x} + \int_{\Omega(t)} \varphi \nabla \cdot ((\mathbf{v} - \mathbf{w})c^f - D\nabla c^f) d\mathbf{x} = 0.$$

We take note that for  $\varphi \in \mathbf{W}(t)$ , we can write  $\hat{\varphi}(\hat{\mathbf{x}}) = \varphi(\mathbf{x}, t) = \varphi(\mathcal{A}_t(\mathbf{x}), t)$ . Here  $\hat{\varphi}$  is the ALE counterpart of  $\varphi$ , and is independent of  $t$ . This means that equation (4) can be written as

$$(5) \quad \int_{\hat{\Omega}} \hat{\varphi} \frac{\partial}{\partial t} (\mathcal{J}_{\mathcal{A}_t} c^f) \Big|_{\hat{\mathbf{x}}} d\hat{\mathbf{x}} + \int_{\Omega(t)} \varphi \nabla \cdot ((\mathbf{v} - \mathbf{w})c^f - D\nabla c^f) d\mathbf{x} = 0.$$

In the first term of equation (5), the time derivative can now be taken outside the integral. This will result in the following

$$(6) \quad \frac{d}{dt} \int_{\Omega(t)} \varphi c^f d\mathbf{x} + \int_{\Omega(t)} \varphi \nabla \cdot ((\mathbf{v} - \mathbf{w})c^f - D\nabla c^f) d\mathbf{x} = 0.$$

At this point, we apply Green's theorem and the boundary conditions (1)<sub>2</sub>, (1)<sub>3</sub>, (1)<sub>4</sub> and (1)<sub>5</sub> to get the conservative variational form:

$$(7) \quad \begin{aligned} & \frac{d}{dt} \int_{\Omega(t)} \varphi c^f d\mathbf{x} - \int_{\Omega(t)} \nabla \varphi \cdot (\tilde{\mathbf{v}} c^f - D\nabla c^f) d\mathbf{x} + \int_{\Sigma(t)} k_d \varphi (\Lambda(c^f) - c^w) d\sigma \\ & + \int_{\Gamma_-(t)} \varphi (\mathbf{v} c_{in}) \cdot \mathbf{n} d\sigma + \int_{\Gamma_+(t)} \varphi (\mathbf{v} c^f) \cdot \mathbf{n} d\sigma = 0. \end{aligned}$$

For the wall solute concentration  $c^w$ , we get the variational form by testing

$$\mathcal{J}_{\mathcal{A}_t}^{-1} \frac{D(\mathcal{J}_{\mathcal{A}_t} c^w)}{Dt} = k_d (\Lambda(c^f) - c^w) \text{ on } \Sigma(t),$$

by  $\psi \in \mathbf{Y}(t)$  to get

$$(8) \quad \frac{d}{dt} \int_{\Sigma(t)} \psi c^w d\sigma = \int_{\Sigma(t)} k_d \psi (\Lambda(c^f) - c^w) d\sigma.$$

Thus, we have:

**Problem 3.1. Conservative formulation.**

Let  $\Lambda \in C^{0,1}(\mathbb{R})$ ,  $\mathcal{A}_t \in \mathbf{W}^{1,\infty}(\hat{\Omega})$ , and  $\mathcal{A}_t^{-1} \in \mathbf{W}^{1,\infty}(\Omega(t))$ . Find a pair  $(c^f, c^w) \in L^2(0, T; \mathbf{W}(t)) \times L^2(0, T; \mathbf{Y}(t))$ , with

$$\frac{d}{dt} \int_{\Omega(t)} c^f \varphi d\mathbf{x}, \frac{d}{dt} \int_{\Sigma(t)} c^w \psi d\sigma \in L^2(0, T),$$

for all  $\varphi \in \mathbf{W}(t)$  and  $\psi \in \mathbf{Y}(t)$ , such that the following equations hold true,

$$(9) \quad \begin{aligned} \frac{d}{dt} \int_{\Omega(t)} c^f \varphi d\mathbf{x} + \mathbf{a}(\varphi, c^f; t) - \int_{\Sigma(t)} k_d \varphi c^w d\sigma &= \mathbf{Q}(\varphi)(t), \\ \frac{d}{dt} \int_{\Sigma(t)} \psi c^w d\sigma + \int_{\Sigma(t)} k_d \psi, c^w d\sigma - \int_{\Sigma(t)} k_d \psi \Lambda(c^f) d\sigma &= 0, \end{aligned}$$

for all  $(\varphi, \psi) \in \mathbf{W}(t) \times \mathbf{Y}(t)$ , where

$$\begin{aligned} \mathbf{a}(\varphi, c^f; t) &= \int_{\Gamma_+(t)} \varphi (\mathbf{v} c^f) \cdot \mathbf{n} d\sigma - \int_{\Omega(t)} \nabla \varphi \cdot ((\mathbf{v} - \mathbf{w}) c^f) d\mathbf{x} + \int_{\Omega(t)} \nabla \varphi \cdot (D \nabla c^f) d\mathbf{x} + \int_{\Sigma(t)} k_d \varphi \Lambda(c^f) d\sigma, \\ \mathbf{Q}(\varphi) &= - \int_{\Gamma_-(t)} (\mathbf{v} c_{in}) \cdot \mathbf{n} \varphi d\sigma. \end{aligned}$$

Note that since  $c^f \in L^2(0, T; \mathbf{W}(t))$ , then  $\Lambda(c^f) \in L^2(0, T; \mathbf{W}(t))$ . Therefore  $\Lambda(c^f)|_{\Sigma(t)} \in L^2(0, T; H^{\frac{1}{2}}(\Sigma(t)))$ .

We will numerically implement the conservative ALE formulation of the problem, using finite element discretization on moving meshes. This is presented in the next section.

#### 4. NUMERICAL SCHEMES

In this section we present the numerical discretization in space and time of the conservative variational formulation on moving meshes. First, we discretize the spatial computational domain to get the computational mesh which is time dependent. The fully discrete mesh can then be obtained through a discretization of the time interval  $[0, T]$ .

We first recall the reference domain  $\hat{\Omega}$ , and the corresponding moving domain  $\Omega(t)$ , as defined earlier. In this numerical implementation, the ALE map describing  $\Omega(t)$  is explicitly given by

$$(10) \quad \mathcal{A}_t : (\hat{x}, \hat{y})^T \mapsto (x, y)^T, \quad \text{where } x = \hat{x}, \quad y = \hat{y} \frac{H + \eta(\hat{x}, t)}{H},$$

for  $(\hat{x}, \hat{y}) \in \hat{\Omega}$ , and  $t \in [0, T]$ . Notice only the radial movement due to this ALE mapping.

To get the spatial discretization of the moving domain  $\Omega(t)$ , we make use of the ALE mapping and start by partitioning the fixed reference domain  $\hat{\Omega}$  into a finite number of triangular elements  $K$  such that

$$(11) \quad \text{cl}(\hat{\Omega}) = \bigcup_{K \in \mathcal{T}_h} K,$$

where  $\text{cl}(\hat{\Omega})$  is the closure of  $\hat{\Omega}$ , and

$$h = \max_K \sup_{\mathbf{x}, \mathbf{y} \in K} \|\mathbf{x} - \mathbf{y}\|_{l^2(\mathbb{R}^2)}.$$

The collection  $\mathcal{T}_h$  is called a *triangulation* of  $\hat{\Omega}$ , with mesh size  $h$ . This triangulation is assumed to be admissible. This means,

- $K$  is a 2D simplex with non-empty interior ( $\text{int}(K) \neq \emptyset$ ),
- $\text{int}(K_1) \cap \text{int}(K_2) = \emptyset$ , for distinct  $K_1, K_2 \in \mathcal{T}_h$ ,
- if  $e = K_1 \cap K_2 \neq \emptyset$ , then  $e$  is an edge or a vertex of  $K_1$  and  $K_2$ , where  $K_1, K_2 \in \mathcal{T}_h$ .

The discrete fixed mesh is given by  $\hat{\Omega}_h = \{\hat{\mathbf{x}}_i : i = 1, \dots, \mathcal{N}_{h_1}\}$ , where  $\mathcal{N}_{h_1}$  is the total number of mesh nodes (mesh size), and  $\hat{\mathbf{x}}_i \in \text{cl}(\hat{\Omega})$ , for each  $i = 1, \dots, \mathcal{N}_{h_1}$ .

Next, we define the moving mesh  $\Omega_h(t)$  which is constructed from the fixed reference mesh  $\hat{\Omega}_h$ . For each  $\mathbf{x}_i(t) \in \Omega_h(t)$ , there is a  $\hat{\mathbf{x}}_i \in \hat{\Omega}_h$ , such that  $\mathbf{x}_i(t) = \mathcal{A}_t(\hat{\mathbf{x}}_i)$ , for  $i = 1, \dots, \mathcal{N}_{h_1}$ . This defines a discrete ALE mapping denoted by  $\mathcal{A}_{h,t}$ . This discrete ALE mapping gives us the triangular elements  $K_t = \mathcal{A}_{h,t}(K)$  on

the moving mesh  $\Omega_h(t)$ , hence the moving mesh triangulation  $\mathcal{T}_{h,t}$  ( see Figure 4 ). In terms of the fixed reference mesh nodes, the moving mesh nodes  $\{\mathbf{x}_i(t)\}_{i=1}^{\mathcal{N}_{h_1}}$  are described via (10).

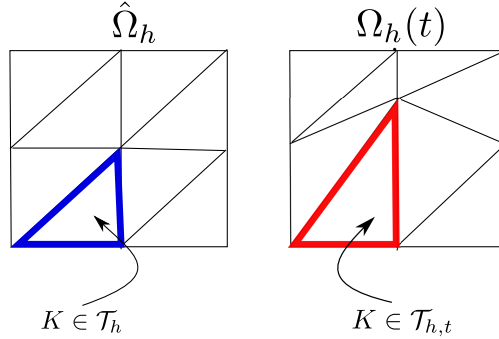


**Figure 4.** The fixed mesh triangulation  $\mathcal{T}_h$ , and the moving mesh triangulation  $\mathcal{T}_{h,t}$ . These are related by the discrete ALE map, as  $\mathcal{T}_{h,t} = \mathcal{A}_{h,t}(\mathcal{T}_h)$ .

For the time discretization, we partition the time interval  $[0, T]$  into the following set of equidistant points

$$\{t^0 \leq t^1 \leq \dots \leq t^{\mathcal{N}_T}\},$$

where  $t^0 = 0$ , and  $t^{\mathcal{N}_T} = T$ . The time-step is then given by  $\Delta t = t^{n+1} - t^n$ . This means that we can now define the fully discrete moving mesh  $\Omega_h^n = \Omega_h(t^n)$ , at  $t = t^n$ . The nodes of this fully discrete mesh are given by  $\mathbf{x}_i^n$ , for  $i = 1, \dots, \mathcal{N}_{h_1}$ . In this fully discrete case, the motion of a moving node from mesh  $\Omega_h^n$  at  $t^n$ , to mesh  $\Omega_h^{n+1}$  at  $t^{n+1}$ , is given by the following linear reconstruction

$$\mathbf{x}_i(t) = \frac{t^{n+1} - t}{\Delta t} \mathbf{x}_i^n + \frac{t - t^n}{\Delta t} \mathbf{x}_i^{n+1}, \quad t \in (t^n, t^{n+1}).$$

We are now in a position to discretize the variational weak formulation in space using the finite element method to get a semi-discrete scheme. With the above linear reconstruction, the geometric conservation law is theoretically satisfied with second order time discretization of the semi-discrete problem [52].

**4.1. Discretization in space.** We now present the finite element discretization of the conservative variational formulation (9). First, we present the finite element space on the reference mesh, and then construct using the discrete ALE map, the finite element spaces on the moving mesh. Let  $P_1(K)$  be the set of first degree polynomials on  $K \in \mathcal{T}_h$ . Therefore, we can define the finite element space for the bulk solute concentration to be

$$\hat{\mathbf{W}}_h := \{\hat{\varphi}_h : \hat{\Omega} \rightarrow \mathbb{R} : \hat{\varphi}_h|_K \in P_1(K) \text{ for all } K \in \mathcal{T}_h\}.$$

For each  $t$ , we write the finite element space defined on the moving domain  $\Omega(t)$ , as

$$\mathbf{W}_h(t) := \{\varphi_h : \Omega(t) \rightarrow \mathbb{R} : \varphi_h \circ \mathcal{A}_{h,t} = \hat{\varphi}_h, \hat{\varphi}_h \in \hat{\mathbf{W}}_h\}.$$

We now define the finite element space for the wall concentration  $c^w$ . Let  $\mathcal{E}_h$  be the set of edges of the triangulation  $\mathcal{T}_h$ . Denote by  $\mathcal{E}_h^w \subset \mathcal{E}_h$  the set of edges lying on the upper (moving) wall  $\hat{\Sigma}$ . We denote the set of those mesh nodes by  $\hat{\Sigma}_h$ , and its size by  $\mathcal{N}_{h_2}$ . We can define a finite element space on the edges  $E \in \mathcal{E}_h^w$  lying on  $\hat{\Sigma}$  as follows:

$$\hat{\mathbf{Y}}_h := \{\hat{\psi}_h : \hat{\Sigma} \rightarrow \mathbb{R} : \hat{\psi}_h|_E \in P_1(E), E \in \mathcal{E}_h^w\}.$$

On the moving domain, we denote by  $\mathcal{E}_{h,t}$  the collection of edges of the elements  $\mathcal{T}_{h,t}$ , and the upper wall moving mesh edges to be  $\mathcal{E}_{h,t}^w$ . The corresponding finite element space defined on the upper wall moving mesh  $\Sigma_h(t)$  with edges  $E \in \mathcal{E}_{h,t}^w$  will be

$$\mathbf{Y}_h(t) := \{\psi_h : \Sigma_h(t) \rightarrow \mathbb{R} : \psi_h \circ \mathcal{A}_{h,t} = \hat{\psi}_h, \hat{\psi}_h \in \hat{\mathbf{Y}}_h\}.$$

Let  $\{\varphi_h^i\}$  be the finite element basis functions for  $\mathbf{W}_h(t)$ , and let  $\{\psi_h^i\}$  be the basis functions for  $\mathbf{Y}_h(t)$ . A basis function  $\psi_i$  of  $\mathbf{Y}_h(t)$ , is clearly a restriction of a function in  $\{\varphi_h^k\}$ , on  $\Sigma_h(t)$ .

From the above definition, we know that  $\varphi_h^i(\mathbf{x}, t) = \hat{\varphi}_h^i(\hat{\mathbf{x}})$  where  $\mathbf{x} = \mathcal{A}_{h,t}(\hat{\mathbf{x}})$ . Similarly,  $\psi_h^i(\mathbf{x}, t) = \hat{\psi}_h^i(\hat{\mathbf{x}})$  where  $\mathbf{x} = \mathcal{A}_{h,t}(\hat{\mathbf{x}}) \in E_t$ , for all  $E_t \in \mathcal{E}_{h,t}^w$ . Let  $\varphi_h \in \{\varphi_h^i\}$  and  $\psi_h \in \{\psi_h^i\}$ . Also define  $c_h^f(\mathbf{x}, t) = \sum_j^{\mathcal{N}_{h_1}} \varphi_h^j(\mathbf{x}, t) c_j^f(t)$  and  $c_h^w(\mathbf{x}, t) = \sum_k^{\mathcal{N}_{h_2}} \psi_h^k(\mathbf{x}, t) c_k^w(t)$ .  $c_j^f(t)$  and  $c_j^w(t)$  are the unknown nodal values of the approximation to  $c^f$ , and  $c^w$  respectively. The numbers  $\mathcal{N}_{h_1}$  and  $\mathcal{N}_{h_2}$ , are clearly the dimensions of  $\mathbf{W}_h(t)$  and  $\mathbf{Y}_h(t)$ , respectively.

The problem in the conservative finite element formulation can be written as follows: For each  $t \in (0, T]$ , find  $(c_h^f, c_h^w) \in \mathbf{W}_h(t) \times \mathbf{Y}_h(t)$  satisfying

$$(12) \quad \begin{cases} \frac{d}{dt} \int_{\Omega(t)} c_h^f \varphi_h d\mathbf{x} + \mathbf{a}(\varphi_h, c_h^f; t) - \int_{\Sigma(t)} k_d \varphi_h c_h^w d\sigma = \mathbf{Q}(\varphi_h), \\ \frac{d}{dt} \int_{\Sigma(t)} c_h^w \psi_h d\sigma + \int_{\Sigma(t)} k_d \psi_h c_h^w d\sigma - \int_{\Sigma_h(t)} k_d \psi_h \Lambda(c_h^f) d\sigma = 0, \end{cases}$$

for all  $\varphi_h \in \mathbf{W}_h(t)$ , and  $\psi_h \in \mathbf{Y}_h(t)$ , where

$$\begin{aligned} \mathbf{a}(\varphi_h, c_h^f; t) &= \int_{\Gamma_+(t)} \varphi_h (\mathbf{v} c^f)_h \cdot \mathbf{n} d\sigma - \int_{\Omega(t)} \left[ \nabla \varphi_h \cdot ((\mathbf{v} - \mathbf{w}) c^f)_h - \nabla \varphi_h \cdot (D \nabla c_h^f) \right] d\mathbf{x} + \int_{\Sigma(t)} k_d \varphi_h \Lambda(c_h^f) d\sigma, \\ \mathbf{Q}(\varphi_h) &= - \int_{\Gamma_-(t)} (\mathbf{v} c_{in}) \cdot \mathbf{n} \varphi_h d\sigma. \end{aligned}$$

In this formulation, we use the group finite element formulation introduced by Fletcher [28]. This method is used to discretize convection terms. Particularly, we will have

$$(\mathbf{v} c^f)_h \approx \sum_i \varphi_h^i c_i^f \mathbf{v}_i, \quad ((\mathbf{v} - \mathbf{w}) c^f)_h \approx \sum_i \varphi_h^i c_i^f (\mathbf{v}_i - \mathbf{w}_i).$$

The compact form of the above finite element discretization is given by,

$$(13) \quad \begin{cases} \frac{d}{dt} [\mathbf{M}_f(t) \mathbf{C}_f(t)] = [\mathbf{K}(t) + \mathbf{S}(t)] \mathbf{C}_f(t) - k_d \mathbf{\Lambda}(\mathbf{C}_f(t)) + k_d \tilde{\mathbf{M}}_w(t) \mathbf{C}_w(t) + \mathbf{Q}(t), \\ \text{for, } t \in (0, T], \mathbf{C}_f(0) = \mathbf{C}_{f,0}, \end{cases}$$

and

$$(14) \quad \begin{cases} \frac{d}{dt} [\mathbf{M}_w(t) \mathbf{C}_w(t)] = k_d \tilde{\mathbf{\Lambda}}(\mathbf{C}_f(t)) - k_d \mathbf{M}_w(t) \mathbf{C}_w(t), \quad t \in (0, T], \\ \mathbf{C}_w(0) = \mathbf{C}_{w,0}, \end{cases}$$

where  $\mathbf{C}_f(t) = \{c_i^f(t)\}_{i=1}^{\mathcal{N}_{h_1}}$ ,  $\mathbf{C}_w(t) = \{c_i^w(t)\}_{i=1}^{\mathcal{N}_{h_2}}$ , and

$$\left\{ \begin{array}{l} \mathbf{M}_f(t) = \{m_{ij}^f(t)\}, \quad m_{ij}^f(t) = \int_{\Omega(t)} \varphi_h^i \varphi_h^j d\mathbf{x}, \\ \mathbf{K}(t) = \{k_{ij}(t)\}, \quad k_{ij}(t) = -(\mathbf{w}_j - \mathbf{v}_j) \cdot \int_{\Omega(t)} \nabla \varphi_h^i \varphi_h^j d\mathbf{x} - \mathbf{v}_j \cdot \int_{\Gamma_+(t)} \varphi_h^i \varphi_h^j \mathbf{n} d\sigma, \\ \mathbf{S}(t) = \{s_{ij}(t)\}, \quad s_{ij}(t) = - \int_{\Omega(t)} \nabla \varphi_h^i \cdot (D \nabla \varphi_h^j) d\mathbf{x} \\ \mathbf{M}_w(t) = \{m_{ij}^w(t)\}, \quad m_{ij}^w(t) = \int_{\Sigma(t)} \psi_h^i \psi_h^j d\sigma \\ \tilde{\mathbf{M}}_w(t) = \{\tilde{m}_{ij}^w(t)\}, \quad \tilde{m}_{ij}^w(t) = \int_{\Sigma(t)} \varphi_h^i \psi_h^j d\sigma \\ \mathbf{Q}(t) = \{q_i(t)\}, \quad q_i(t) = - \int_{\Gamma_-(t)} \varphi_h^i (\mathbf{v} c_{in})_h \cdot \mathbf{n} d\sigma, \\ \mathbf{\Lambda}(\mathbf{C}_f(t)) = \{\lambda_i(\mathbf{C}_f(t))\}_i, \quad \lambda_i(\mathbf{C}_f(t)) = \int_{\Sigma(t)} \varphi_h^i \Lambda \left( \sum_j c_j^f(t) \varphi_h^j \right) d\sigma, \\ \tilde{\mathbf{\Lambda}}(\mathbf{C}_f(t)) = \{\tilde{\lambda}_i(\mathbf{C}_f(t))\}_i, \quad \tilde{\lambda}_i(\mathbf{C}_f(t)) = \int_{\Sigma(t)} \psi_h^i \Lambda \left( \sum_j c_j^f(t) \varphi_h^j \right) d\sigma. \end{array} \right.$$

In addition, we have the initial condition for the semi-discrete problem:  $\mathbf{C}_f(0) = \mathbf{C}_{f,0} = \{c_0^f(\mathbf{x}_i)\}_i$  with a similar form for  $\mathbf{C}_w(0)$ . In this formulation,  $\mathbf{M}_w(t)$  is an  $\mathcal{N}_{h_2} \times \mathcal{N}_{h_2}$  wall mass matrix which is invertible. On the other hand,  $\tilde{\mathbf{M}}_w(t)$  is a  $\mathcal{N}_{h_1} \times \mathcal{N}_{h_2}$  rectangular matrix with extra zero rows for nodes not on  $\Sigma_h(t)$ . In that sense,  $\tilde{\mathbf{M}}_w(t)$  is an extension of  $\mathbf{M}_w(t)$  onto the entire  $\Omega_h(t)$ . Also, here we used  $\tilde{\mathbf{\Lambda}}$  to denote a restriction of  $\mathbf{\Lambda}$  to the nodes on  $\Sigma_h(t)$  with size  $\mathcal{N}_{h_2} \times 1$ .

This semi-discrete problem is a semi-linear problem, with the nonlinearity appearing only in the chemical reaction term  $\mathbf{\Lambda}$ . We deal with this nonlinearity by constructing the so called Patankar linearization approach.

**4.2. Discretization in time: Patankar linearization.** In this section we present a time discretization scheme for the coupled problem via a Patankar type approach for linearizing the nonlinear reaction terms [16]. This helps us avoid the costly Newton type linearization which is not mass conservative. We note that these schemes have been studied for general production-destruction models in [16–18, 46]. A positivity preserving TVD type scheme for treating problems with convection and possible dominant reaction in reactive transport processes was studied in detail in [46]. The most comprehensive study of Patankar schemes is found in [16] for various time integration schemes, such as backward and forward Euler and Runge-Kutta schemes. What is most encouraging is the unconditional positivity preservation, mass conservation, and second order consistency for the Runge-Kutta type scheme, as seen in Theorem 3.6 in [16]. In [32], a similar study is considered which extends the results in [16] to more general time integration schemes. We will briefly introduce a general description of the scheme for a general production-destruction problem. First, consider the following general coupled production-destruction problem

$$(15) \quad \left\{ \begin{array}{l} \frac{d\xi(t)}{dt} = \mathbf{P}(\xi) - \mathbf{D}(\xi), \quad \xi(0) = \xi_0, \\ \xi = (\xi_1, \dots, \xi_I)^T, \quad t \in (0, T]. \end{array} \right.$$

The production  $\mathbf{P}$ , and destruction  $\mathbf{D}$  terms are componentwise positive, and can be written in component form as follows

$$(16) \quad P_i(\boldsymbol{\xi}) = \sum_{j=1, j \neq i}^I p_{i,j}(\boldsymbol{\xi}), \quad D_i(\boldsymbol{\xi}) = \sum_{j=1, j \neq i}^I d_{i,j}(\boldsymbol{\xi}).$$

where  $p_{i,j}(\boldsymbol{\xi}) \geq 0$  is the rate of mass transfer by reaction from component  $j$  to component  $i$ . The rate  $d_{i,j}(\boldsymbol{\xi})$  is for the mass transfer from component  $j$  to component  $i$ . It should be noted that  $p_{i,i}(\boldsymbol{\xi})$ , and  $d_{i,i}(\boldsymbol{\xi})$  are due to production or destruction of the  $i$ th component without influence of the  $j$ th component. In conservative models, this should not be the case, thus  $p_{i,i}(\boldsymbol{\xi}) = d_{i,i}(\boldsymbol{\xi}) = 0$ .

We introduce the time splitting Patankar linearization scheme. The first half-step is the forward Euler-Patankar scheme. This is followed by a Crank-Nicolson-Patankar scheme, also known as a midpoint rule Patankar scheme. The elements of this scheme are modifications of the traditional Patankar schemes found in [16]. The scheme is defined as follows:

$$(17) \quad \begin{aligned} \xi_i^{n+\frac{1}{2}} &= \xi_i^n + \frac{\Delta t}{2} \left( \sum_{j=1, j \neq i}^I \tilde{p}_{i,j}(\boldsymbol{\xi}^n) \xi_j^n - \sum_{j=1, j \neq i}^I \tilde{d}_{i,j}(\boldsymbol{\xi}^n) \xi_i^n \right), \quad i = 1, \dots, I, \\ \xi_i^{n+1} &= \xi_i^n + \Delta t \left( \sum_{j=1, j \neq i}^I \tilde{p}_{i,j}(\boldsymbol{\xi}^{n+\frac{1}{2}}) \left[ \frac{\xi_j^n + \xi_j^{n+1}}{2} \right] - \sum_{j=1, j \neq i}^I \tilde{d}_{i,j}(\boldsymbol{\xi}^{n+\frac{1}{2}}) \left[ \frac{\xi_i^n + \xi_i^{n+1}}{2} \right] \right), \quad i = 1, \dots, I, \end{aligned}$$

where  $t^{n+\frac{1}{2}} = \frac{t^n + t^{n+1}}{2}$ ,  $\tilde{p}_{i,j}(\boldsymbol{\xi}) = \frac{p_{i,j}(\boldsymbol{\xi})}{\xi_i}$ , and  $\tilde{d}_{i,j}(\boldsymbol{\xi}) = \frac{d_{i,j}(\boldsymbol{\xi})}{\xi_i}$ , for  $j \neq i$ . We will perform the Patankar linearization for our problem in the semi-linear, semi-discrete equations (12). There will be two unknowns, namely  $\xi_1(t)$  and  $\xi_2(t)$ . These are given by,

$$(18) \quad \xi_1(t) = \mathbf{M}_f(t) \mathbf{C}_f(t), \quad \xi_2(t) = \mathbf{M}_w(t) \mathbf{C}_w(t).$$

These variables will correspond to the two different components in the Patankar scheme. We also define  $\tilde{\xi}_2(t) = \tilde{\mathbf{M}}_w(t) \mathbf{C}_w(t)$  to be the extension of  $\xi_2(t)$  to the whole mesh  $\Omega_h(t)$ . The size of  $\tilde{\xi}_2(t)$  is  $\mathcal{N}_{h_1} \times 1$ . Then, we can write problem (13), (14) by introducing the following notation in terms of production-destruction functions:

$$(19) \quad \begin{aligned} p_{1,2}(\boldsymbol{\xi}(t)) &= k_d \tilde{\xi}_2(t), \\ d_{1,2}(\boldsymbol{\xi}(t)) &= \left\{ \int_{\Sigma(t)} \varphi_h^i k_d \Lambda \left( \sum_j \varphi_h^j c_j^f(t) \right) d\sigma \right\}_{i=1}^{\mathcal{N}_{h_1}}, \\ p_{2,1}(\boldsymbol{\xi}(t)) &= \left\{ \int_{\Sigma(t)} \psi_h^i k_d \Lambda \left( \sum_j \varphi_h^j c_j^f(t) \right) d\sigma \right\}_{i=1}^{\mathcal{N}_{h_2}}, \\ d_{2,1}(\boldsymbol{\xi}(t)) &= k_d \xi_2(t). \end{aligned}$$

Now to approximate the nonlinear adsorption, introduce the Patankar linearization in the weak form, defining  $\tilde{d}_{1,2}$  and  $\tilde{p}_{2,1}$  in the following way:

$$(20) \quad \begin{aligned} \tilde{d}_{1,2}(\boldsymbol{\xi}(t)) \xi_1(t) &= \left\{ \sum_j \int_{\Sigma(t)} \varphi_h^i \varphi_h^j k_d \frac{\Lambda(c_h^f(\mathbf{x}, t))}{c_h^f(\mathbf{x}, t)} c_j^f(t) d\sigma \right\}_{i=1}^{\mathcal{N}_{h_1}} \\ &= \mathbf{R}(\mathbf{C}_f(t)) \mathbf{C}_f(t), \quad t \in [0, T], \end{aligned}$$

$$(21) \quad \begin{aligned} \tilde{p}_{2,1}(\boldsymbol{\xi}(t))\xi_1(t) &= \left\{ \sum_j \int_{\Sigma(t)} \psi_h^i \varphi_h^j k_d \frac{\Lambda(c_h^f(\mathbf{x}, t))}{c_h^f(\mathbf{x}, t)} c_j^f(t) d\sigma \right\}_{i=1}^{N_{h_2}} \\ &= \tilde{\mathbf{R}}(\mathbf{C}_f(t))\mathbf{C}_f(t), \quad t \in [0, T], \end{aligned}$$

where  $\mathbf{R}(\mathbf{C}_f(t))$  and  $\tilde{\mathbf{R}}(\mathbf{C}_f(t))$  will be evaluated using the previously calculated values of  $\mathbf{C}_f(t)$ . Since  $\Lambda$  is Lipschitz, the fraction  $\Lambda(c_h^f)/c_h^f$  is well defined. Therefore  $\tilde{d}_{1,2}$  and  $\tilde{p}_{2,1}$  are bounded. Let us now denote by  $\mathbf{R}(t) := \mathbf{R}(\mathbf{C}_f(t))$  and  $\tilde{\mathbf{R}}(t) := \tilde{\mathbf{R}}(\mathbf{C}_f(t))$  the linearized isotherm matrices from the Patankar linearization, then we have the following linear semidiscrete scheme:

$$(22) \quad \begin{aligned} \frac{d}{dt}[\mathbf{M}_f(t)\mathbf{C}_f(t)] &= [\mathbf{K}(t) + \mathbf{S}(t) - \mathbf{R}(t)]\mathbf{C}_f(t) + k_d\tilde{\mathbf{M}}_w(t)\mathbf{C}_w(t) + \mathbf{Q}(t), \\ \frac{d}{dt}[\mathbf{M}_w(t)\mathbf{C}_w(t)] &= \tilde{\mathbf{R}}(t)\mathbf{C}_f(t) - k_d\mathbf{M}_w(t)\mathbf{C}_w(t), \quad t \in (t^n, t^{n+1}), \\ \mathbf{C}_f(0) &= \mathbf{C}_{f,0}, \quad \mathbf{C}_w(0) = \mathbf{C}_{w,0}, \end{aligned}$$

where  $\mathbf{R}(t)$  and  $\tilde{\mathbf{R}}(t)$  are calculated from known values of  $\mathbf{C}_f(t)$ .

**Remark 4.1.** For linear isotherms  $\Lambda$  the Patankar trick is not necessary, and  $\mathbf{R}(t)$  will be equivalent to  $k_a\mathbf{M}_w(t)$  which is independent of  $\mathbf{C}_f(t)$ , where  $k_a$  is the adsorption rate. Other than this difference, the rest of the scheme remains unchanged.

4.2.1. *Fully discrete Patankar-Galerkin scheme.* We design a direct high order predictor-corrector scheme, which is obtained by a half step forward Euler-Patankar scheme, a Crank-Nicholson-Galerkin scheme, and a midpoint scheme. They are summarized below.

**Step 1: Compute auxiliary wall and bulk solute concentrations.**

We compute the auxiliary wall and bulk solute concentration by a half step forward Euler scheme.

$$(23) \quad \begin{cases} \mathbf{M}_w^{n+\frac{1}{2}}\mathbf{C}_w^{n+\frac{1}{2}} = \mathbf{M}_w^n\mathbf{C}_w^n + \frac{\Delta t}{2} [\tilde{\mathbf{R}}^n\mathbf{C}_f^n - k_d\mathbf{M}_w^n\mathbf{C}_w^n], \\ \mathbf{M}_f^{n+\frac{1}{2}}\mathbf{C}_f^{n+\frac{1}{2}} = \mathbf{M}_f^n\mathbf{C}_f^n + \frac{\Delta t}{2} [\mathbf{K}^n + \mathbf{S}^n - \mathbf{R}^n]\mathbf{C}_f^n + \frac{\Delta t}{2} k_d\tilde{\mathbf{M}}_w^n\mathbf{C}_w^n + \frac{\Delta t}{2}\mathbf{Q}^n. \end{cases}$$

**Remark 4.2.** For the linear isotherm case, equation (23)<sub>2</sub> is not required as it is only for the half step updating of  $\mathbf{R}^{n+\frac{1}{2}} := \mathbf{R}(\mathbf{C}_f^{n+\frac{1}{2}})$ , which we use below.

**Step 2: Compute the final bulk solute concentration  $\mathbf{C}_f^{n+1}$  at  $t^{n+1}$ .**

We approximate the bulk solute concentration at  $t^{n+1}$  by the Crank-Nicholson-Patankar (CNP) scheme:

$$(24) \quad \begin{cases} \mathbf{A}^{n+1}\mathbf{C}_f^{n+1} = \mathbf{B}^n\mathbf{C}_f^n + k_d\Delta t\tilde{\mathbf{M}}_w^{n+\frac{1}{2}}\mathbf{C}_w^{n+\frac{1}{2}} + \Delta t\mathbf{Q}^{n+\frac{1}{2}}, \\ \text{where,} \\ \mathbf{A}^{n+1} = \mathbf{M}_f^{n+1} - \frac{\Delta t}{2}(\mathbf{K}^{n+\frac{1}{2}} + \mathbf{S}^{n+\frac{1}{2}} - \mathbf{R}^{n+\frac{1}{2}}), \\ \mathbf{B}^n = \mathbf{M}_f^n + \frac{\Delta t}{2}(\mathbf{K}^{n+\frac{1}{2}} + \mathbf{S}^{n+\frac{1}{2}} - \mathbf{R}^{n+\frac{1}{2}}). \end{cases}$$

**Step 3: Compute final wall concentration at  $t^{n+1}$  by a midpoint rule.** This is obtained as follows:

$$(25) \quad \mathbf{M}_w^{n+1}\mathbf{C}_w^{n+1} = \mathbf{M}_w^n\mathbf{C}_w^n + \frac{\Delta t}{2}\tilde{\mathbf{R}}^{n+\frac{1}{2}}(\mathbf{C}_f^n + \mathbf{C}_f^{n+1}) - \Delta t k_d\mathbf{M}_w^{n+\frac{1}{2}}\mathbf{C}_w^{n+\frac{1}{2}}.$$

**4.3. ALE-FCT scheme.** We present a linearized FCT algorithm that closely follows the standard roadmap for FCT schemes (see [41], [42], [11]). The scheme is introduced to ensure positivity preservation and mass conservation. The FCT scheme is a predictor-corrector scheme with two parts. The first part is an approximation of the solution using a low order scheme. This low order solution is then corrected using a flux limiting strategy in the second part.

We now derive the low order approximation following the standard FCT roadmap. We start by introducing the lumped mass matrix in the place of  $\mathbf{M}_f(t)$ , which is defined by  $\mathbf{M}_{Lf}(t) = \text{diag}(m_i^f(t))$ , where  $m_i^f(t) = \sum_j m_{ij}^f(t)$ . This will remove the off-diagonal positive entries, yet still ensuring mass conservation and the robustness of the linear system. Respectively, we can write the lumped matrix for  $\mathbf{M}_w(t)$  as  $\mathbf{M}_{Lw}(t)$ , which is defined in a similar way. We also introduce an artificial diffusion operator  $\mathbf{D}(t)$ , and define the low order discrete convection operator as  $\mathbf{L}(t) = \mathbf{K}(t) + \mathbf{D}(t)$ , where  $\mathbf{D}(t)$  is calculated as follows:

$$(26) \quad \begin{cases} \mathbf{D}(t) = \{d_{ij}(t)\}, & \text{where} \\ d_{ij}(t) = \max\{-k_{ij}(t), 0, -k_{ji}(t)\}, & \text{for } j \neq i \\ d_{ii}(t) = -\sum_{j \neq i} d_{ij}(t) & \text{for all } i. \end{cases}$$

The artificial diffusion operator renders  $\mathbf{L}(t)$  positivity-preserving and removes the entries of the matrix  $\mathbf{K}(t)$  that violate the positivity constraint.

Similarly, the linearized reaction term is lumped to get  $\mathbf{R}_L(t)$ . This step is optional in general, but is necessary for the reaction dominated case. In this discussion we will treat the problem as a convection and reaction dominated process.

In fully discrete form, the low order scheme, obtained by the above matrix manipulations, for the bulk solute concentration reads as follows: Find  $\mathbf{C}_f^L$  such that:

$$(27) \quad \begin{aligned} \mathbf{M}_{Lf}^{n+1} \mathbf{C}_f^L &= \mathbf{M}_{Lf}^n \mathbf{C}_f^n + \frac{\Delta t}{2} (\mathbf{L}^{n+\frac{1}{2}} + \mathbf{S}^{n+\frac{1}{2}} - \mathbf{R}_L^{n+\frac{1}{2}}) \mathbf{C}_f^n \\ &+ \frac{\Delta t}{2} (\mathbf{L}^{n+\frac{1}{2}} + \mathbf{S}^{n+\frac{1}{2}} - \mathbf{R}_L^{n+\frac{1}{2}}) \mathbf{C}_f^L + k_d \Delta t \tilde{\mathbf{M}}_{Lw}^{n+\frac{1}{2}} \mathbf{C}_w^{n+\frac{1}{2}} + \Delta t \mathbf{Q}^{n+\frac{1}{2}}, \end{aligned}$$

where  $\mathbf{C}_f^L$  is calculated on the mesh  $\Omega_h^{n+1}$ . This is the predictor step. The low order bulk solute concentration  $\mathbf{C}_f^L$  will be positive for sufficiently small  $\Delta t$ . However, this scheme is highly diffusive, and less accurate, because of the added artificial diffusion. Thus the solution will have to be corrected. The corrector step is

$$\mathbf{M}_{Lf}^{n+1} \mathbf{C}_f^{n+1} = \mathbf{M}_{Lf}^{n+1} \mathbf{C}_f^L + \Delta t \bar{\mathbf{f}}, \quad \text{where } \bar{\mathbf{f}} = \sum_{j \neq i} \alpha_{ij} f_{ij}.$$

Here  $\alpha_{ij}$  will be determined through the Zalesak flux limiting strategy, presented in section 4.3.2, and  $f_{ij}$  are computed from the antidiffusive component given by

$$(28) \quad \mathbf{f} = (\mathbf{M}_{Lf}^{n+1} - \mathbf{M}_{Lf}^{n+1}) \dot{\mathbf{C}}_f^L - [\mathbf{D}^{n+1} - (\mathbf{R}_L^L - \mathbf{R}^L)] \mathbf{C}_f^L,$$

where we used  $\dot{\mathbf{C}}_f^L$  to denote an approximation to the time derivative of  $\mathbf{C}_f^L$ .

To decompose  $\mathbf{f}$  into the internodal fluxes  $f_{ij}$ , we first note the following decompositions,

$$\begin{aligned} [(\mathbf{M}_{L_f}^{n+1} - \mathbf{M}_f^{n+1})\dot{\mathbf{C}}_f^L]_i &= \sum_{j \neq i} (m_{ij}^f)^{n+1} (\dot{c}_{f,i}^L - \dot{c}_{f,j}^L), \quad i \in \{1, \dots, \mathcal{N}_{h_1}\}, \\ [(\mathbf{R}_L^L - \mathbf{R}^L)\mathbf{C}_f^L]_i &= \sum_{j \neq i} r_{ij}^L (c_{f,i}^L - c_{f,j}^L), \quad i \in \{1, \dots, \mathcal{N}_{h_1}\}, \\ [\mathbf{D}^{n+1}\mathbf{C}_f^L]_i &= - \sum_{j \neq i} d_{ij}^{n+1} (c_{f,i}^L - c_{f,j}^L), \quad i \in \{1, \dots, \mathcal{N}_{h_1}\}. \end{aligned}$$

So we can now write  $\mathbf{f}_i = \sum_{j \neq i} f_{ij}$ , where  $f_{ij}$  are given by

$$(29) \quad f_{ij} = (m_{ij}^f)^{n+1} (\dot{c}_{f,i}^L - \dot{c}_{f,j}^L) + (d_{ij}^{n+1} + r_{ij}^L) (c_{f,i}^L - c_{f,j}^L).$$

The time derivative approximation  $\dot{\mathbf{C}}_f^L = \{\dot{c}_{f,i}^L\}_i$ , is calculated as in [11, 41], as follows,

$$(30) \quad \mathbf{M}_f^{n+1} \dot{\mathbf{C}}_f^L = [\mathbf{K}^{n+1} + \mathbf{S}^{n+1} - \mathbf{R}^L] \mathbf{C}_f^L + k_d \tilde{\mathbf{M}}_w^{n+1} \mathbf{C}_w^{n+1} + \mathbf{Q}^{n+1},$$

or the less computationally demanding

$$(31) \quad \mathbf{M}_{L_f}^{n+1} \dot{\mathbf{C}}_f^L = [\mathbf{K}^{n+1} + \mathbf{S}^{n+1} - \mathbf{R}^L] \mathbf{C}_f^L + k_d \tilde{\mathbf{M}}_w^{n+1} \mathbf{C}_w^{n+1} + \mathbf{Q}^{n+1}.$$

We should note that the convection operator  $\mathbf{K}^{n+1}$  is calculated on the new mesh  $\Omega_h^{n+1}$ , with the velocity  $\mathbf{v}^{n+\frac{1}{2}} - \mathbf{w}^{n+\frac{1}{2}}$  at  $t^{n+\frac{1}{2}}$ , because of the jump at  $t^{n+1}$  of the mesh velocity  $\mathbf{w}_j(t) = \frac{\mathbf{x}_j^{n+1} - \mathbf{x}_j^n}{\Delta t}$ ,  $t \in [t^n, t^{n+1})$ . The reaction matrix  $\mathbf{R}^L$  is also calculated on the new mesh  $\Omega_h^{n+1}$ , using the positive low order bulk solute concentration  $\mathbf{C}_f^L$ .

The wall solute concentration  $\mathbf{C}_w^{n+1}$ , will be calculated using the following lumped system

$$(32) \quad \mathbf{M}_{L_w}^{n+1} \mathbf{C}_w^{n+1} = \mathbf{M}_{L_w}^n \mathbf{C}_w^n + \frac{\Delta t}{2} \tilde{\mathbf{R}}_L^{n+\frac{1}{2}} (\mathbf{C}_f^n + \mathbf{C}_f^L) - \Delta t k_d \mathbf{M}_{L_w}^{n+\frac{1}{2}} \mathbf{C}_w^{n+\frac{1}{2}}.$$

This calculation will guarantee that the final wall solute concentration is positive, provided  $\Delta t$  is small enough.

The next subsection summarizes the above derivation into the steps that must be followed in the implementation.

#### 4.3.1. *Algorithm: An ALE-FCT-Patankar scheme.*

**Step 1: Compute wall and bulk solute concentration by a half step forward Euler scheme:**

$$(33) \quad \begin{cases} \mathbf{M}_{L_w}^{n+\frac{1}{2}} \mathbf{C}_w^{n+\frac{1}{2}} = \mathbf{M}_{L_w}^n \mathbf{C}_w^n + \frac{\Delta t}{2} [\tilde{\mathbf{R}}_L^n \mathbf{C}_f^n - k_d \mathbf{M}_{L_w}^n \mathbf{C}_w^n], \\ \mathbf{M}_{L_f}^{n+\frac{1}{2}} \mathbf{C}_f^{n+\frac{1}{2}} = \mathbf{M}_{L_f}^n \mathbf{C}_f^n + \frac{\Delta t}{2} [\mathbf{L}^n + \mathbf{S}^n - \mathbf{R}_L^n] \mathbf{C}_f^n \\ \quad + \frac{\Delta t}{2} k_d \tilde{\mathbf{M}}_{L_w}^n \mathbf{C}_w^n + \frac{\Delta t}{2} \mathbf{Q}^n. \end{cases}$$

**Step 2: Compute the low order bulk solute concentration  $\mathbf{C}_f^L$  at  $t^{n+1}$  by a Crank-Nicholson scheme:**

$$(34) \quad \begin{cases} \mathbf{G}^{n+1} \mathbf{C}_f^L = \mathbf{H}^n \mathbf{C}_f^n + \Delta t k_d \tilde{\mathbf{M}}_{L_w}^{n+\frac{1}{2}} \mathbf{C}_w^{n+\frac{1}{2}} + \Delta t \mathbf{Q}^{n+\frac{1}{2}}, \\ \text{where,} \\ \mathbf{G}^{n+1} = \mathbf{M}_{L_f}^{n+1} - \frac{\Delta t}{2} [\mathbf{L}^{n+\frac{1}{2}} + \mathbf{S}^{n+\frac{1}{2}} - \mathbf{R}_L^{n+\frac{1}{2}}], \\ \mathbf{H}^n = \mathbf{M}_{L_f}^n + \frac{\Delta t}{2} [\mathbf{L}^{n+\frac{1}{2}} + \mathbf{S}^{n+\frac{1}{2}} - \mathbf{R}_L^{n+\frac{1}{2}}]. \end{cases}$$

**Step 3: Compute final wall solute concentration at  $t^{n+1}$  by a midpoint rule scheme:**

$$(35) \quad \mathbf{M}_{Lw}^{n+1} \mathbf{C}_w^{n+1} = \mathbf{M}_{Lw}^n \mathbf{C}_w^n + \frac{\Delta t}{2} \tilde{\mathbf{R}}_L^{n+\frac{1}{2}} [\mathbf{C}_f^n + \mathbf{C}_f^L] - \Delta t k_d \mathbf{M}_{Lw}^{n+\frac{1}{2}} \mathbf{C}_w^{n+\frac{1}{2}}.$$

**Step 4: Compute the final bulk solute concentration by algebraic flux correction:**

$$(36) \quad \mathbf{M}_{Lf}^{n+1} \mathbf{C}_f^{n+1} = \mathbf{M}_{Lf}^{n+1} \mathbf{C}_f^L + \Delta t \bar{\mathbf{f}}.$$

**4.3.2. Zalesak flux limiting strategy.** The following is a Zalesak multidimensional flux limiting procedure for moving mesh simulations. This algorithm first proposed in [62], studied in the finite element context in [40, 41], and extended to moving meshes in [11], is applied to our correction step, which is **step 4** above.

**Step 0: Prelimiting step (Optional)** If  $f_{ij}$  has the same sign as  $c_{f,j}^L - c_{f,i}^L$  then  $f_{ij}$  is antidiffusive in nature and might flatten the solution profile instead of steepening it. We cancel such fluxes by checking if  $f_{ij}(c_{f,j}^L - c_{f,i}^L) > 0$  and if this is true, set  $f_{ij} = 0$ .

**Step 1:** Compute sums of the positive and negative fluxes to each node. These represent the total positive and negative contributions to node  $i$  from neighboring nodes at the end of each time step:

$$P_i^+ = \sum_{j \neq i} \max\{0, f_{ij}\}, \quad P_i^- = \sum_{j \neq i} \min\{0, f_{ij}\}.$$

**Step 2:** Compute the distance to the local extremum of the auxiliary solution  $\mathbf{C}_f^L$ . This is done by considering the neighboring nodes to get

$$Q_i^+ = \max\{0, \max_{j \neq i} (c_{f,j}^L - c_{f,i}^L)\}, \quad Q_i^- = \min\{0, \min_{j \neq i} (c_{f,j}^L - c_{f,i}^L)\}.$$

**Step 3:** Compute the nodal correction factors for net increment at node  $i$ . These are the ratios of the net fluxes and the distance to the local extremum as follows:

$$R_i^+ = \min \left\{ 1, \frac{(m_i^f)^{n+1} Q_i^+}{\Delta t P_i^+} \right\}, \quad R_i^- = \min \left\{ 1, \frac{(m_i^f)^{n+1} Q_i^-}{\Delta t P_i^-} \right\}.$$

**Step 4:** Compute  $\alpha_{ij}$

$$\alpha_{ij} = \begin{cases} \min\{R_i^+, R_j^-\}, & \text{if } f_{ij} > 0, \\ \min\{R_i^-, R_j^+\}, & \text{if } f_{ij} \leq 0. \end{cases}$$

This completes the derivation of the full linearized ALE-FCT scheme for solving the reactive transport problem in moving domains.

We show next that the algorithm is both mass conservative, and positivity preserving.

**4.3.3. Mass conservation of the ALE-FCT scheme.** Mass conservation is one of the most essential features of the algorithm. In the continuous case, we expect that, in the absence of fluxes across the boundary,

$$\frac{d}{dt} \int_{\Omega(t)} c^f(\mathbf{x}, t) d\mathbf{x} + \frac{d}{dt} \int_{\Sigma(t)} c^w(\mathbf{x}, t) d\sigma = 0.$$

For the fully discrete case at  $t = t^n$ , we have the mass for the bulk solute concentration given by  $\sum_i (\mathbf{M}_{Lf}^n \mathbf{C}_f^n)_i$ , and for the wall solute concentration by  $\sum_i (\mathbf{M}_{Lw}^n \mathbf{C}_w^n)_i$ . This is the quantity that has to stay constant in time only to be affected by flux across the boundary.

**Theorem 4.1.** *The ALE-FCT scheme is conservative in the sense that the net change in the total mass is only dependent on the flux across the boundary. Thus, we have*

$$\sum_i \{\mathbf{M}_{Lf}^{n+1} \mathbf{C}_f^{n+1} - \mathbf{M}_{Lf}^n \mathbf{C}_f^n\}_i + \sum_i \{\mathbf{M}_{Lw}^{n+1} \mathbf{C}_w^{n+1} - \mathbf{M}_{Lw}^n \mathbf{C}_w^n\}_i = \sum_i \{\mathbf{K}_+^{n+\frac{1}{2}} (\mathbf{C}_f^L + \mathbf{C}_f^n)\}_i + \Delta t \sum_i \mathbf{Q}_i^{n+\frac{1}{2}},$$

where  $\mathbf{K}_+^{n+\frac{1}{2}}$  is the coefficient matrix of the flux across  $\Gamma_+(t^{n+\frac{1}{2}})$ , and  $\mathbf{Q}_i^{n+\frac{1}{2}}$  is the inlet flux on  $\Gamma_-(t^{n+\frac{1}{2}})$ .

*Proof.* The difference between the total mass at  $t^{n+1}$  and  $t^n$  is computed as follows:

$$\begin{aligned}
& \sum_i \{M_{L_f}^{n+1} C_f^{n+1} - M_{L_f}^n C_f^n\}_i + \sum_i \{M_{L_w}^{n+1} C_w^{n+1} - M_{L_w}^n C_w^n\}_i \\
&= \sum_i \{M_{L_f}^{n+1} C_f^L + \Delta t \bar{f} - M_{L_f}^n C_f^n\}_i + \sum_i \left\{ \frac{\Delta t}{2} \tilde{\mathbf{R}}_L^{n+\frac{1}{2}} (C_f^n + C_f^L) - \Delta t k_d M_{L_w}^{n+\frac{1}{2}} C_w^{n+\frac{1}{2}} \right\}_i + \sum_i \Delta t Q_i^{n+\frac{1}{2}} \\
&= \sum_i \left\{ \frac{\Delta t}{2} (\mathbf{L}^{n+\frac{1}{2}} + \mathbf{S}^{n+\frac{1}{2}} - \mathbf{R}_L^{n+\frac{1}{2}}) C_f^L + [M_{L_f}^n + \frac{\Delta t}{2} (\mathbf{L}^{n+\frac{1}{2}} + \mathbf{S}^{n+\frac{1}{2}} - \mathbf{R}_L^{n+\frac{1}{2}})] C_f^n \right. \\
&\quad \left. + \Delta t k_d \tilde{M}_{L_w}^{n+\frac{1}{2}} C_w^{n+\frac{1}{2}} + \Delta t \bar{f} - M_{L_f}^n C_f^n \right\}_i + \sum_i \left\{ \frac{\Delta t}{2} \tilde{\mathbf{R}}_L^{n+\frac{1}{2}} (C_f^n + C_f^L) - \Delta t k_d M_w^{n+\frac{1}{2}} C_w^{n+\frac{1}{2}} \right\}_i + \sum_i \Delta t Q_i^{n+\frac{1}{2}} \\
&= \sum_i \left\{ \frac{\Delta t}{2} (\mathbf{L}^{n+\frac{1}{2}} + \mathbf{S}^{n+\frac{1}{2}}) (C_f^L + C_f^n) + \Delta t \bar{f} \right\}_i + \sum_i \Delta t Q_i^{n+\frac{1}{2}}.
\end{aligned}$$

Note that  $\sum_i \bar{f}_i = \sum_i \sum_{j \neq i} f_{ij} \alpha_{ij}$  and  $f_{ij} = -f_{ji}$ ,  $\alpha_{ij} = \alpha_{ji}$ . This implies that  $\sum_i \bar{f}_i = 0$ . Moreover,

$$\sum_i [\mathbf{S}^{n+\frac{1}{2}} C_f]_i = \sum_i \sum_j s_{ij}^{n+\frac{1}{2}} c_{f,j} = \sum_i \sum_{j \neq i} s_{ij}^{n+\frac{1}{2}} (c_{f,j} - c_{f,i}) = 0,$$

as  $s_{ij}^{n+\frac{1}{2}} = s_{ji}^{n+\frac{1}{2}}$ . Similarly,  $\sum_i (\mathbf{D}^{n+\frac{1}{2}} C_f)_i = 0$  as  $\mathbf{D}$  is a diffusion operator. The remaining convection term can be written as  $\mathbf{K}^{n+\frac{1}{2}} = \mathbf{K}_{int}^{n+\frac{1}{2}} + \mathbf{K}_+^{n+\frac{1}{2}}$ , where

$$[\mathbf{K}_{int}^{n+\frac{1}{2}}]_{ij} = -(\mathbf{w}_j - \mathbf{v}_j) \cdot \int_{\Omega(t^{n+\frac{1}{2}})} \nabla \varphi_i \varphi_j d\mathbf{x}, \quad \text{and} \quad [\mathbf{K}_+^{n+\frac{1}{2}}]_{ij} = -\mathbf{v}_j \cdot \int_{\Gamma_+(t^{n+\frac{1}{2}})} \varphi_i \varphi_j n d\sigma.$$

As a result

$$(37) \quad \sum_i [\mathbf{K}_{int}^{n+\frac{1}{2}} C_f]_i = \sum_j -(\mathbf{w}_j - \mathbf{v}_j) \cdot \int_{\Omega(t^{n+\frac{1}{2}})} \left( \sum_i \nabla \varphi_i \right) \varphi_j c_{f,j} d\mathbf{x} = 0.$$

Therefore, we get

$$\sum_i \{M_{L_f}^{n+1} C_f^{n+1} - M_{L_f}^n C_f^n\}_i + \sum_i \{M_{L_w}^{n+1} C_w^{n+1} - M_{L_w}^n C_w^n\}_i = \sum_i \{ \mathbf{K}_+^{n+\frac{1}{2}} (C_f^L + C_f^n) \}_i + \Delta t \sum_i Q_i^{n+\frac{1}{2}}.$$

□

**4.3.4. Positivity preservation.** In this section we provide a rigorous analysis of the numerical scheme, and derive a sufficient conditions for the scheme to be positivity preserving. This condition is written in terms of a restriction on the time step  $\Delta t$ . First, we note that Zalesak's limiter is designed to guarantee that the flux-corrected solution is bounded by the local maxima and minima of the low order predictor. Hence, positivity of the low-order scheme implies that of the full ALE-FCT scheme.

In order for positivity to be preserved in the low-order scheme, we need for  $\mathbf{G}^{n+1}$  to be an *M-matrix* and for  $\mathbf{H}^n$  to have non-negative entries. Recall that an M-matrix is a monotone matrix with non-positive off-diagonal entries. A sufficient condition for this is a matrix with positive diagonal entries, non-positive off-diagonal entries and strict or irreducible diagonal dominance. The diagonal and off-diagonal entries for these matrices are given, respectively, by

$$\left\{ \begin{array}{l} G_{ii}^{n+1} = (m_i^f)^{n+1} - \frac{\Delta t}{2}(l_{ii}^{n+\frac{1}{2}} + s_{ii}^{n+\frac{1}{2}} - r_i^{n+\frac{1}{2}}), \\ G_{ij}^{n+1} = -\frac{1}{2}\Delta t(l_{ij}^{n+\frac{1}{2}} + s_{ij}^{n+\frac{1}{2}}), \end{array} \right. \quad \text{and} \quad \left\{ \begin{array}{l} H_{ii}^n = (m_i^f)^n + \frac{\Delta t}{2}(l_{ii}^{n+\frac{1}{2}} + s_{ii}^{n+\frac{1}{2}} - r_i^{n+\frac{1}{2}}), \\ H_{ij}^n = \frac{1}{2}\Delta t(l_{ij}^{n+\frac{1}{2}} + s_{ij}^{n+\frac{1}{2}}). \end{array} \right.$$

Given a node  $i$ , we define  $S_i = \{j \neq i : G_{ij}^{n+1} \neq 0, \text{ or } H_{ij}^n \neq 0\}$ , which is the set of neighboring nodes on the moving mesh. For  $\mathbf{G}^{n+1}$  to be an M-matrix, we need  $G_{ii}^{n+1} > 0$  and  $G_{ij}^{n+1} \leq 0$  for  $j \in S_i$ . This is satisfied automatically in this case, thanks to the artificial diffusion added to  $\mathbf{K}^{n+\frac{1}{2}}$  to give  $\mathbf{L}^{n+\frac{1}{2}}$ . For  $\mathbf{H}^n$  to have non-negative entries, we need  $\Delta t$  small enough. The following CFL type condition will suffice

$$(38) \quad \Delta t \leq \min_i \frac{2(m_i^f)^n}{r_i^{n+\frac{1}{2}} - l_{ii}^{n+\frac{1}{2}} - s_{ii}^{n+\frac{1}{2}}}.$$

Additionally, we have a condition on  $\Delta t$  that guarantees positivity of the auxiliary wall concentration. It is given by

$$\Delta t \leq \frac{2}{k_d}.$$

The third constraint on  $\Delta t$  is due to the explicit initial update of the bulk fluid concentration in step 1. This update is positivity-preserving under the CFL-like condition

$$(39) \quad \Delta t \leq \min_i \frac{2(m_i^f)^n}{r_i^n - l_{ii}^n - s_{ii}^n},$$

which has the same structure as (38), and is derived in the same way.

To derive a time step constraint for the calculation of the final wall concentration  $\mathbf{C}_w^{n+1}$ , we substitute the product  $\mathbf{M}_{Lw}^{n+1/2} \mathbf{C}_w^{n+1/2}$  given by (33) into (35), and obtain

$$\begin{aligned} \mathbf{M}_{Lw}^{n+1} \mathbf{C}_w^{n+1} &= \mathbf{M}_{Lw}^n \mathbf{C}_w^n + \frac{\Delta t}{2} \tilde{\mathbf{R}}_L^{n+1/2} [\mathbf{C}_f^n + \mathbf{C}_f^L] - \Delta t k_d \left[ \mathbf{M}_{Lw}^n \mathbf{C}_w^n + \frac{\Delta t}{2} [\tilde{\mathbf{R}}_L^n \mathbf{C}_f^n - k_d \mathbf{M}_{Lw}^n \mathbf{C}_w^n] \right] \\ &= \left[ 1 - \Delta t k_d + \frac{(\Delta t k_d)^2}{2} \right] \mathbf{M}_{Lw}^n \mathbf{C}_w^n + \frac{\Delta t}{2} [\tilde{\mathbf{R}}_L^{n+1/2} - \Delta t k_d \tilde{\mathbf{R}}_L^n] \mathbf{C}_f^n + \frac{\Delta t}{2} \tilde{\mathbf{R}}_L^{n+1/2} \mathbf{C}_f^L, \end{aligned}$$

where  $\mathbf{M}_{Lw}$  and  $\tilde{\mathbf{R}}_L$  are diagonal matrices. It follows that the calculation of  $\mathbf{C}_w^{n+1}$  is positivity-preserving for time steps satisfying

$$(40) \quad \Delta t \leq \min \left\{ \frac{1}{k_d} + k_d \frac{(\Delta t)^2}{2}, \frac{1}{k_d} \min_i \frac{r_i^{n+\frac{1}{2}}}{r_i^n} \right\}.$$

Since the values of  $r_i^{n+\frac{1}{2}}$  depend on  $\mathbf{C}_f^{n+\frac{1}{2}}$ , so does the upper bound for  $\Delta t$ . If  $\tilde{\mathbf{R}}_L^n$  is replaced by  $\tilde{\mathbf{R}}_L^{n+1/2}$  in the first equation of (33), then (35) is equivalent to

$$\begin{aligned} \mathbf{M}_{Lw}^{n+1} \mathbf{C}_w^{n+1} &= \left[ 1 - \Delta t k_d + \frac{(\Delta t k_d)^2}{2} \right] \mathbf{M}_{Lw}^n \mathbf{C}_w^n \\ &\quad + \frac{\Delta t}{2} [1 - \Delta t k_d] \tilde{\mathbf{R}}_L^{n+1/2} \mathbf{C}_f^n + \frac{\Delta t}{2} \tilde{\mathbf{R}}_L^{n+1/2} \mathbf{C}_f^L, \end{aligned}$$

which preserves positivity under the simpler time step restriction

$$(41) \quad \Delta t \leq \frac{1}{k_d}.$$

The final restriction on  $\Delta t$  is then given by

$$(42) \quad \Delta t \leq \min \left\{ \frac{1}{k_d}, \min_i \frac{2(m_i^f)^n}{r_i^n - l_{ii}^n - s_{ii}^n}, \min_i \frac{2(m_i^f)^n}{r_i^{n+\frac{1}{2}} - l_{ii}^{n+\frac{1}{2}} - s_{ii}^{n+\frac{1}{2}}} \right\}.$$

Therefore, we conclude that the scheme is positivity preserving if (42) is satisfied.

## 5. NUMERICAL RESULTS

In this section we present the numerical results for the ALE-FCT scheme. We will first validate the accuracy of the scheme by considering some reactive transport problems in a fixed domain. The numerical results from this scheme will be compared to existing effective models. We will then allow the computational mesh to move, and we will study the extent to which the mesh movement affects our numerical solution. By the *geometric conservation law* (GCL), the mesh movement should not result in a significant change in the numerical solution [57]. The numerical tests will include irreversible wall reactions, linear adsorption-desorption (Henry's law), infinite adsorption, and nonlinear Langmuir adsorption. All of these will be studied in a narrow fixed, semi-infinite channel that characterizes a reactor or a pore.

The second issue to be considered is the grid convergence of the numerical scheme. The numerical solution, calculated on fixed meshes will be compared to a reference solution on a fixed fine mesh. In a moving mesh, the moving mesh solution will be compared to a moving mesh solution on a fine mesh. The CFL number will be kept constant with mesh refinement. In addition, we will also study the moving mesh error by comparing the moving mesh solution on coarse meshes to the fixed mesh solution on a fine mesh. This study will be done for linear adsorption-desorption, and nonlinear Langmuir adsorption.

Finally, we will simulate the reactive transport of a single solute species in a moving domain. We will simulate both linear and nonlinear reactions. The linear reaction will be the Henry's law. The nonlinear reaction will be the Langmuir isotherm. The second case requires Patankar linearization. Our first point of interest will be the positivity and mass conservation of the solution in both linear and nonlinear cases. We will also compare the linear and nonlinear solution. The final part of the moving mesh simulation will be a comparison of the wall solute concentration on fixed vs. moving walls.

**5.1. Reactive transport in a fixed semi-infinite channel.** We begin with a numerical study of the ALE-FCT scheme for the advection-diffusion equation with wall reactions, in a fixed, two dimensional semi-infinite channel. In [25, 27, 60] and [26], effective models for such transport are rigorously derived via anisotropic singular perturbation expansions. These effective models are known as **Taylor-Aris models**. The earliest of such models was established in the classical work by Taylor [59], and generalized by Aris [3]. Using energy estimates, the full 2D model equations were shown to converge to the effective models as  $\varepsilon = H/L_R \rightarrow 0$ , where  $H$  is the channel height,  $L_R$  is observation distance, and  $\varepsilon$  is the aspect ratio [25, 27, 60]. The numerical results of our full simulation are compared with those of the effective one dimensional form of this model.

The full mathematical model for convection-diffusion in a fixed, semi-infinite channel is given in dimensional form by

$$(43) \quad \frac{\partial c^*}{\partial t^*} + q(y^*) \frac{\partial c^*}{\partial x^*} - D^* \Delta_{x^*, y^*} c^* = 0, \quad \text{for,} \quad (x^*, y^*, t^*) \in \mathbb{R}_+ \times (-H, H) \times (0, T^*),$$

$$(44) \quad -D^* \partial_y c^* = \partial_{t^*} \hat{c} = k_d (\Lambda(c^*) - \hat{c}), \quad \text{for,} \quad |y^*| = H, \quad x^* \in \mathbb{R}_+, \quad t^* \in (0, T^*),$$

where  $q(y^*) = Q^*(1 - (y^*/H)^2)$  is the parabolic fluid velocity profile,  $Q^*$  is the characteristic velocity, and  $D^*$  is the molecular diffusion. The Laplace operator is given by  $\Delta_{x^*, y^*} = \partial_{x^* x^*} + \partial_{y^* y^*}$ . Moreover,  $k_d$  is the desorption constant, and  $\Lambda$  is the reaction rate, which may be nonlinear. It should be noted that this is the original problem (1) in a fixed domain, with the velocity profile given to be the Poiseuille profile. The bulk solute concentration is denoted by  $c^*$ , and the wall solute concentration by  $\hat{c}$ .

The objective here is to simulate the reactive transport process in a fixed channel. Only the upper half of the domain will be considered:  $\Omega = (0, L) \times (0, H)$ , because the flow can be taken to be symmetric about

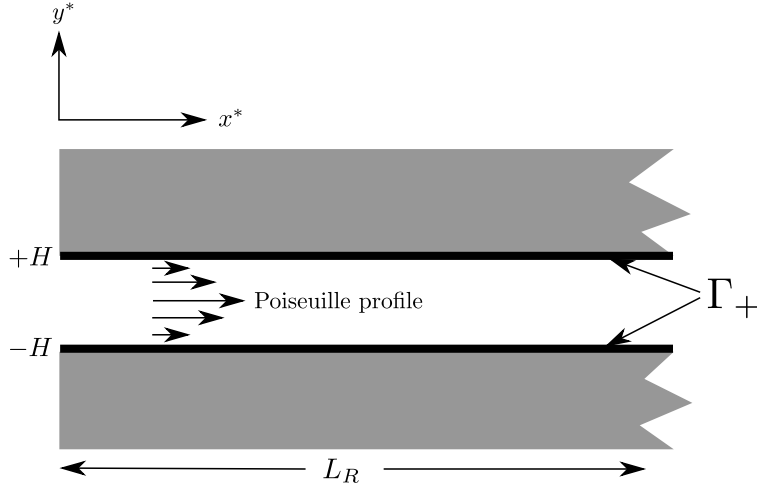


**Figure 5.** The schematics for a fixed narrow channel  $\mathbb{R}_+ \times (-H, H)$ , with wall reactions on  $\Gamma_+$ , and a Poiseuille profile for fluid velocity.

the axis  $y^* = 0$ . Now the wall reaction only occurs on  $y^* = H$ . The length of the channel  $L$ , is taken to be twice the observation distance  $L_R$ , that is,  $L = 2L_R$ . To compute the numerical solution, we discretize the domain  $\Omega$ , to get  $\Omega_h$ . The mesh  $\Omega_h$  has  $n_x \times n_y$  uniform rectangles with logical triangulation. The mesh is defined by  $\Delta x^* = L/n_x$ , and  $\Delta y^* = H/n_y$ . The time step is given by  $\Delta t^*$ .

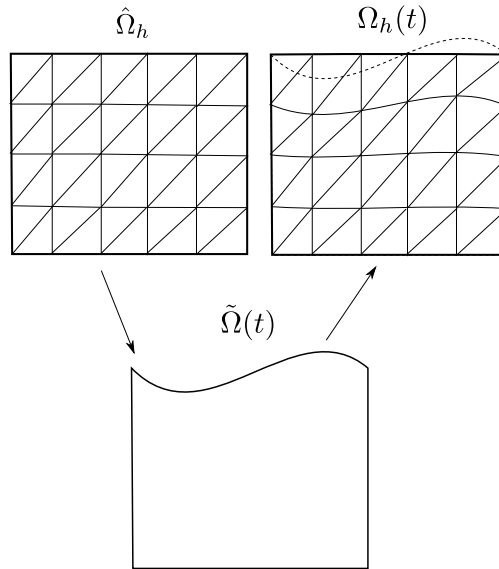


**Figure 6.** The fixed and moving meshes defined on a fixed domain. The moving mesh is defined by a virtual, given vertical deformation function  $\eta(x, t)$ . The fixed mesh is denoted by  $\hat{\Omega}_h = \Omega_h$ , and the moving mesh by  $\Omega_h(t)$ .

To show that the solution does not depend on the moving mesh, we perform our simulations on a fixed domain with both fixed and moving meshes. A comparison between the two solutions provides information about the influence of the mesh motion on the solution accuracy.

For the moving meshes, the problem will be solved using the ALE-FCT scheme. Using the discrete ALE map, we will define the moving mesh  $\Omega_h(t)$ , as a deformation of a fixed reference mesh  $\hat{\Omega}_h$ . In this case, the fixed reference mesh  $\hat{\Omega}_h$ , is given by  $\Omega_h$ .

The deformation of the reference mesh will be defined by the vertical deformation of the upper wall  $y^* = H$ . The top wall in the reference mesh is moved vertically by the function

$$(45) \quad \eta(x^*, t^*) = a \cdot \cos(2\pi x^*) \sin(2\pi t^*),$$

where the amplitude  $a$  of the wall deformation is a fraction of  $\Delta y^*$ . As a result, we get an auxiliary time dependent domain  $\tilde{\Omega}(t^*)$  for  $t^* \geq 0$  as follows

$$(46) \quad \tilde{\Omega}(t^*) := \{x^* \in \mathbb{R}^2 : x^* \in (0, L), y^* \in (0, H + \eta(x^*, t^*))\}.$$

The discrete counterpart of this domain  $\tilde{\Omega}_h(t^*)$  is an  $n_x \times n_y$  mesh that has moving nodes defined by  $\tilde{x}_{ij}^*(t) = i\Delta x^*$  and  $\tilde{y}_{ij}^*(t) = j \cdot \frac{H + \eta(i\Delta x^*, t^*)}{n_y}$ . The result is a moving mesh  $\Omega_h(t^*)$ , defined on the fixed domain, with the nodes given by

$$(47) \quad \begin{aligned} x_{ij}^*(t^*) &= \tilde{x}_{ij}^*(t^*) = i \cdot \Delta x^*, \quad i = 0, \dots, n_x, \quad j = 0, \dots, n_y \\ y_{ij}^*(t^*) &= \begin{cases} \tilde{y}_{ij}^*(t^*), & j = 0, \dots, n_y - 1, \\ H, & j = n_y. \end{cases} \end{aligned}$$

This is achieved by taking the interior nodes of  $\tilde{\Omega}_h(t^*)$ , and superimposing them on  $\Omega$ . The interior nodes are guaranteed to stay within  $\Omega$ , since the vertical movement is strictly less than  $\Delta y^*$ .

5.1.1. *Irreversible wall reaction in a fixed semi-infinite channel.* We consider the reactive transport problem with irreversible reaction on the wall with highly dominant convection. In this case  $k_d \Lambda(c^*) = \hat{k}^* c^*$ , and  $k_d = \hat{k}^*/K_e$ , where  $K_e$  is the equilibrium reaction rate. The wall reaction condition (44) is thus written as

$$(48) \quad -D^* \partial_y c^* = \partial_{t^*} \hat{c} = \hat{k}^* c^* - \hat{k}^* \hat{c}/K_e,$$

for  $y^* = H$ ,  $x^* \in (0, L)$ , and  $t^* \in (0, T^*)$ .

First, we present the effective model for the flow in the semi-infinite channel with the condition given by (48). We introduce the following characteristic variables for non-dimensionalization of our problem:  $L_R$  as above, is the characteristic length, chosen to be the observation distance;  $Q_R$  is the characteristic velocity;  $D_R$  is the characteristic diffusivity; and  $T_R$  is the characteristic time for the whole process.  $T_T$  and  $T_L$  are the transversal and longitudinal timescales, respectively, while  $T_{DE}$  and  $T_A$  are characteristic desorption and adsorption timescales, respectively. The other characteristic variables are given by the subscripted counterparts of their respective dimensional variables. We present these variables as follows

$$\begin{aligned} c^\varepsilon &= \frac{c^*}{c_R}, \quad x = \frac{x^*}{L_R}, \quad t = \frac{t^*}{T_R}, \quad Q = \frac{Q^*}{Q_R}, \quad D = \frac{D^*}{D_R}, \quad T = \frac{T^*}{T_R}, \\ y &= \frac{y^*}{H}, \quad k = \frac{\hat{k}^*}{k_R}, \quad c_s^\varepsilon = \frac{\hat{c}}{\hat{c}_R}, \quad K = \frac{K_e}{K_{eR}}, \quad \alpha = \frac{\log Pe}{\log(1/\varepsilon)}, \end{aligned}$$

where  $Pe = Q^* L_R / D^*$  is the longitudinal Péclet number. Substituting these characteristic variables into (43), we get the following full non-dimensional problem: Find  $(c^\varepsilon, c_s^\varepsilon)$  satisfying

$$\begin{aligned} \frac{\partial c^\varepsilon}{\partial t} + Q(1-y^2) \frac{\partial c^\varepsilon}{\partial x} &= D\varepsilon^\alpha \frac{\partial^2 c^\varepsilon}{\partial x^2} + D\varepsilon^{\alpha-2} \frac{\partial^2 c^\varepsilon}{\partial y^2} \\ c^\varepsilon(x, y, 0) &= 1 \quad , \quad (x, y) \in \mathbb{R}_+ \times (0, 1) \\ -D\varepsilon^{\alpha-2} \frac{\partial c^\varepsilon}{\partial y} &= \frac{T_A}{T_{DE}} \frac{\partial c_s^\varepsilon}{\partial t} = \frac{T_L}{T_{DE}} k \left( c^\varepsilon - \frac{T_A}{T_{DE}} c_s^\varepsilon / K \right) \text{ on } \Gamma^+ \times (0, T) \\ \frac{\partial c^\varepsilon}{\partial y}(x, 0, t) &= 0 \text{ on } (x, t) \in \mathbb{R}_+ \times (0, T), \end{aligned}$$

where  $\Gamma_+ = \{(x, y) : x \in \mathbb{R}_+, y = 1\}$ . The y-average of the solution of this 2D problem can be well approximated, for  $\varepsilon$  small, by the following 1D effective model, first derived in [60], and later rigorously

justified in [26] for linear adsorption-desorption, and in [47] for irreversible kinetics ( $K_e = +\infty$ ):

$$\partial_t \left( c^{eff} + \frac{T_A}{T_{DE}} c_s^{eff} \right) + \left( \frac{2Q}{3} + \frac{2Qk}{45D} \frac{T_T}{T_{DE}} \right) \partial_x c^{eff} - \left( D\varepsilon^\alpha + \frac{8}{945} \frac{Q^2}{D} \varepsilon^{2-\alpha} \right) \partial_{xx} c^{eff} = \frac{2Qk}{45DK} \frac{T_A T_T}{(T_{DE})^2} \partial_x c_s^{eff},$$

$$\left( 1 + \frac{k}{3D} \frac{T_T}{T_{DE}} \right) \partial_t c_s^{eff} = k \frac{T_L}{T_A} \left( c^{eff} + \frac{2Q}{45D} \varepsilon^{2-\alpha} \partial_x c^{eff} - \frac{T_A}{T_{DE}} c_s^{eff} / K \right).$$

This is defined for  $(x, t) \in (0, \infty) \times (0, T)$ . In dimensional form, the effective model can be written as: Find  $(c^*, \hat{c})$  in  $(x^*, t^*) \in \mathbb{R}_+ \times (0, T^*)$  satisfying

$$(49) \quad \begin{cases} \partial_{t^*} \left( c^* + \frac{\hat{c}}{H} \right) + \left( \frac{2Q^*}{3} + \frac{2Q^* Da_T}{45} \right) \partial_{x^*} c^* - D^* \left( 1 + \frac{8}{945} Pe_T^2 \right) \partial_{x^* x^*} c^* = \frac{2Q^* Da_T}{45K_e} \partial_{x^*} \hat{c}, \\ \left( 1 + \frac{1}{3} Da_T \right) \partial_{t^*} \hat{c} = \hat{k}^* \left( c^* + \frac{2HPe_T}{45} \partial_{x^*} c^* - \frac{\hat{c}}{K_e} \right), \end{cases}$$

where  $Pe_T = \frac{Q^* H}{D^*}$  is the transversal Péclet number, and  $Da_T = \frac{\hat{k}^* H}{D^*}$  is the transversal Damköhler number. Note that we are using  $c^*$ , and  $\hat{c}$  here for the effective concentration in  $(x^*, t^*) \in \mathbb{R}_+ \times (0, T^*)$ .

In this section, we specifically study the irreversible wall reactions, i.e.,  $K_e = +\infty$ . Therefore, the effective model for this problem is given by

$$(50) \quad \partial_{t^*} c^* + \left( \frac{2Q^*}{3} + \frac{4Q^* Da_T}{45} \right) \partial_{x^*} c^* + \frac{\hat{k}^*}{H} \left( 1 - \frac{Da_T}{3} \right) c^* - D^* \left( 1 + \frac{8}{945} Pe_T^2 \right) \partial_{x^* x^*} c^* = 0, \text{ in } (0, +\infty) \times (0, T).$$

The effective model has an explicit solution, which is given by

$$(51) \quad c^*(x^*, t^*) = e^{-k_1 t^*} \left\{ 1 - \frac{1}{\sqrt{\pi}} \left( e^{\frac{2Q_1 x^*}{3D_1}} \int_{\frac{x^* + 2t^* Q_1/3}{2\sqrt{D_1 t^*}}}^{\infty} e^{-\eta^2} d\eta + \int_{\frac{x^* - 2t^* Q_1/3}{2\sqrt{D_1 t^*}}}^{\infty} e^{-\eta^2} d\eta \right) \right\},$$

where  $k_1 = \frac{\hat{k}^*}{H} \left( 1 - \frac{Da_T}{3} \right)$ ,  $Q_1 = Q^* \left( 1 + \frac{2Da_T}{15} \right)$ , and  $D_1 = D^* \left( 1 + \frac{8}{945} Pe_T^2 \right)$ . This represents an approximation of the cross sectional average of the  $2D$  solution.

In the numerical experiment that follows, the  $1D$  explicit solution (51) is compared to the cross-sectional average of a  $2D$  solution obtained using the standard FEM, to the average of the  $2D$  solution obtained using the FEM-FCT on a fixed mesh, and to the average of the  $2D$  solution obtained using the ALE-FCT on a moving mesh. The initial and boundary data are given by  $c^*|_{x^*=0} = 0$ , and  $c^*|_{t^*=0} = 1$ , respectively. The full simulation, with the characteristic time of 100 seconds, is performed with the data given in Table 1. The reaction rate is given by  $\hat{k}^* = Q^*/400$ .

**Table 1.** Parameter values for first order irreversible surface reaction ( $K_e = \infty$ )

Parameters	Values
Width of the slit: $H$	$2.635 \times 10^{-4}$ m
Characteristic length: $L_R$	0.632 m
$\varepsilon = H/L_R$	$0.41693 \times 10^{-3}$
Characteristic velocity: $Q^*$	$0.393 \times 10^{-2}$ m/s
Diffusion coefficient: $D^*$	$1.2 \times 10^{-8}$ m <sup>2</sup> /s
Longitudinal Péclet number: $Pe = L_R Q^*/D^*$	$2.0698 \times 10^5$
$\alpha = \log Pe / \log(1/\varepsilon)$	1.572789
Transversal Péclet number: $Pe_T = H Q^*/D^*$	86.296
Transversal Damköhler number: $Da_T = \hat{k}^* H/D^*$	0.2157

In this simulation we first consider a comparison between the effective  $1D$  model, the standard FEM  $2D$  solution and the  $2D$  FEM-FCT solution. This is done on a fixed mesh. The simulation is done first on a

coarse mesh with  $\Delta x^* = L/100$ ,  $\Delta y^* = H/10$  and  $\Delta t^* = 0.01$ . We refine once to get the finer mesh with  $(\frac{\Delta x^*}{2}, \frac{\Delta y^*}{2}, \frac{\Delta t^*}{2})$ . The mesh Péclet numbers on the coarse and fine meshes are given by  $Pe_h = \frac{\Delta x^* Q^*}{D^*} = 2.0698 \times 10^3$  and  $Pe_{h/2} = \frac{\Delta x^* Q^*}{2D^*} = 1.035 \times 10^3$ , respectively, showing convection dominance. The results for this are illustrated in Figure 7. The positions of the steep fronts obtained using both numerical schemes (standard FEM and FEM-FCT) are in agreement with those of the 1D effective model. The average of the 2D solution from the standard FEM scheme performs very poorly compared to the average of the 2D solution from the FEM-FCT scheme. There is a slight improvement to the average solution from the standard FEM scheme when we refine once.

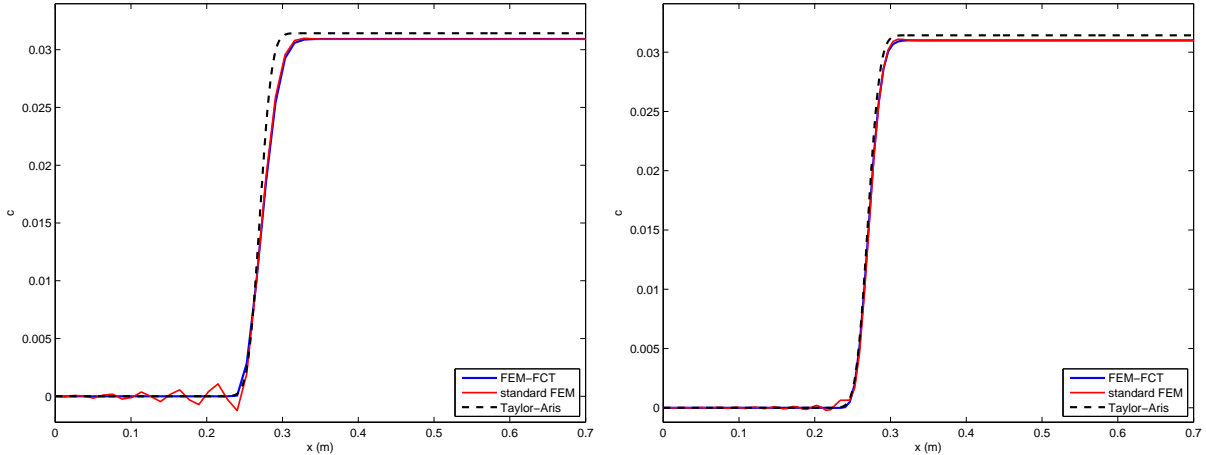


**Figure 7. Irreversible wall reaction; fixed channel case and fixed mesh.** Comparison between the cross-sectional average of a solution obtained using the standard FEM Galerkin scheme (solid blue), the FEM-FCT scheme (solid red), and the effective 1D explicit solution of the **Taylor-Aris model** (dashed line), at time  $t = 100$  seconds. Left figure shows the simulation on the coarse mesh, the right figure shows the simulation on a fine mesh.

The next step is the moving mesh simulation. We take the parameters to be the same as in the fixed mesh case. The mesh deformation is defined by the function (45), with the amplitude taken to be  $a = \Delta y/30$ . The simulation results are shown in Figure 8. Here we compare the 1D explicit solution of the effective model to the averaged 2D numerical solutions from standard ALE-FEM scheme and the ALE-FCT scheme. The ALE-FEM solution, as with its fixed mesh counterpart, performs poorly with oscillations in the vicinity of the steep front. The ALE-FCT scheme, gives us well resolved fronts with no oscillations. Upon refinement, the ALE-FEM solution improves, but is still worse than ALE-FCT, as there are small oscillations present. The numerical solution in the moving mesh case also shows excellent agreement with the effective 1D model. This means that the mesh deformation does not significantly affect the numerical solution.

In this section, we simulated transport with irreversible wall reactions. The FCT scheme performed very well on both fixed and moving meshes compared to the standard FEM scheme. Also, the numerical solution was in very good agreement with the explicit solution of the 1D effective Taylor-Aris model. We next consider a slightly more diffusive case, involving reversible linear adsorption-desorption wall reactions.

**5.1.2. Linear adsorption-desorption in a fixed semi-infinite channel.** In this section we study the reactive transport with linear adsorption-desorption on the wall of the fixed channel  $\mathbb{R}_+ \times (-H, H)$ . The transport will be slight more diffusive than in the case of irreversible reactions in section 5.1.1. The computational domain is  $\Omega = (0, L) \times (0, H)$ , as in section 5.1.1, with axial symmetry on  $y^* = 0$ . On the wall of the channel  $y^* = \pm H$  we have the linear adsorption-desorption described by

$$(52) \quad -D^* \partial_{y^*} c^* = \frac{\partial \hat{c}}{\partial t^*} = \hat{k}^* (c^* - \hat{c}/K_e),$$

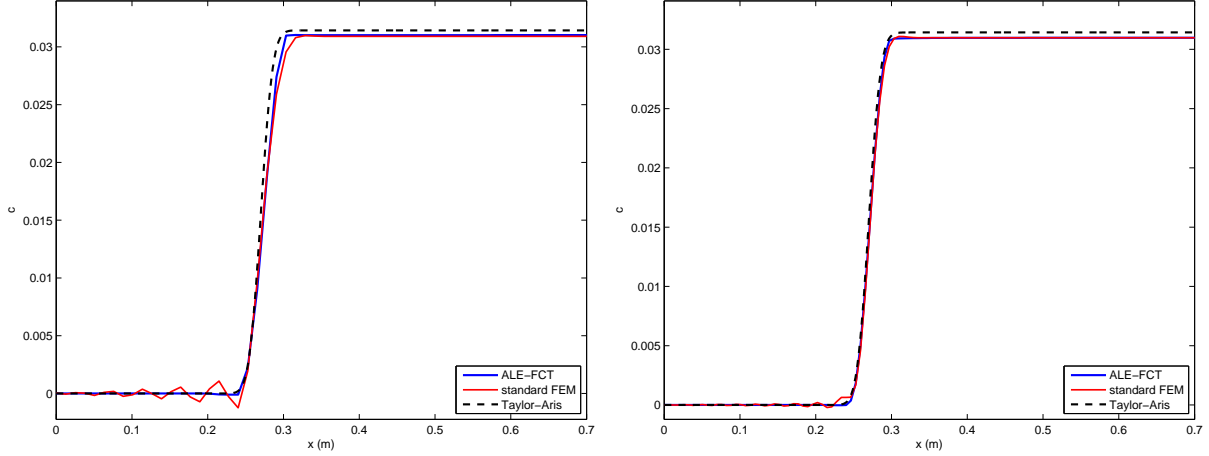


**Figure 8. Irreversible wall reaction; fixed channel case and moving mesh.** Comparison between the cross-sectional average of a solution obtained using the standard ALE-FEM scheme (solid red), the ALE-FCT scheme (solid blue), and the effective 1D explicit solution of the **Taylor-Aris model** (dashed line), at time  $t = 100$  seconds. Left figure shows the simulation on the coarse mesh, the right figure shows the simulation on a fine mesh. The mesh is moving with amplitude  $a = \Delta y/30$ .

where  $\hat{k}^*, K_e < +\infty$ .

In the numerical experiments that follow, we will compare the average of the numerical solution of the full 2D problem given by (43) and (52), to the solution of the 1D effective Taylor-Aris model (49). The effective model (49), however, has no explicit solution when  $K_e < \infty$ , which is our case now. Therefore, we will compare the averaged 2D numerical solution obtained using the FEM-FCT scheme to the 1D numerical solution of the effective model, obtained using a finite difference scheme. Moreover, we will simulate transport on moving meshes defined on the fixed domain to show that the implementation of the FEM-FCT scheme for the adsorption-desorption problem is independent of the mesh motion.

A simulation with a characteristic time of 350 seconds is performed using the data in Table 2. In this case the reaction parameters from scaling are given by  $\hat{k}^* = \varepsilon Q^*$  and  $K_e = H$ . The simulation times of interest are  $t^* = 100, 211$  and 350 seconds. The inlet boundary condition for this problem is  $c^*(0, t^*) = 1$ , and the initial condition is  $c^*(x^*, 0) = 0$ . The mesh parameters for the mesh are given by  $\Delta x^* = L/150$ ,  $\Delta y^* = H/30$  and  $\Delta t^* = 0.1$ , where  $L = 2L_R$  is the channel length. The mesh Péclet number is given by  $Pe_h = 126.4$ . The CFL number is given by  $CFL = \frac{Q^* \Delta x}{\Delta t} = 0.035601$ , which is fairly small.

**Table 2.** Full linear wall adsorption-desorption parameters

Parameters	Values
Width of the slit: $H$	$0.5 \times 10^{-2}$ m
Characteristic length: $L_R$	0.632 m
$\varepsilon = \frac{H}{L_R}$	$0.7911 \times 10^{-2}$
Characteristic velocity: $Q^*$	$0.3 \times 10^{-2}$ m/s
Diffusion coefficient: $D^*$	$0.2 \times 10^{-6}$ m <sup>2</sup> /s
Longitudinal Péclet number: $Pe = L_R Q^*/D^*$	$9.48 \times 10^3$
$\alpha = \log Pe / \log(1/\varepsilon)$	1.670972
Transversal Péclet number: $Pe_T = H Q^*/D^*$	75
Characteristic reaction velocity: $\hat{k}^* = \varepsilon Q^*$	$0.237 \times 10^{-4}$ m/s
Transversal Damköhler number: $Da_T = \varepsilon(H Q^*/D^*)$	0.5933

The results for the fixed and moving mesh simulations are shown in Figure 9. There is very good agreement between the 2D full model numerical result, and the 1D effective model result. The effective model is of order  $O(\varepsilon^{2(2-\alpha)})$ , and this corresponds to approximately 0.0414 asymptotic error. Corresponding to this, we look at the point-wise error

$$E(x^*) = \left[ c_{effective}^*(x^*, T^*) - \frac{1}{H} \int_0^H c_{full}^*(x^*, y^*, T^*) dy^* \right],$$

between the effective model  $c_{effective}^*$ , and the averaged full model  $c_{full}^*$ . For the fixed mesh we have the error within  $[-0.0273, 0.0065]$ , and for the moving mesh we have the error to be within  $[-0.0270, 0.0052]$ . These values are less than the asymptotic error, or are of the same order as the asymptotic error. This means that there is very good agreement between the 1D effective model, and the 2D numerical scheme for both fixed and moving meshes.

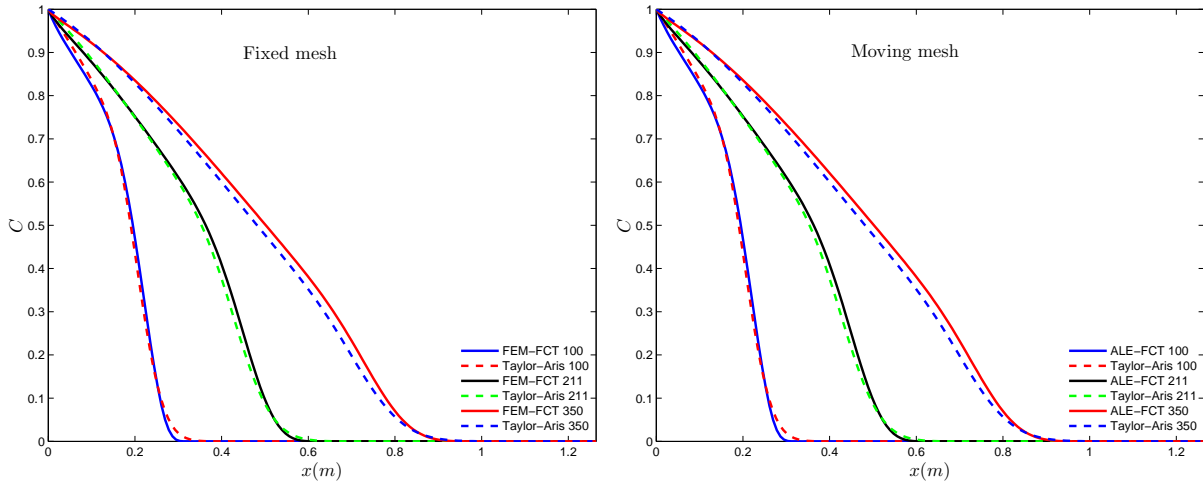


**Figure 9. Linear adsorption-desorption; fixed channel, fixed (left) and moving (right) meshes.** Left: Comparison between the cross-sectional average of a solution obtained using the full FCT scheme (solid line) and the effective Taylor-Aris model (dashed line) on a fixed mesh. Right: Comparisons between the cross-sectional average of a solution obtained using the ALE-FCT scheme (solid line) and the effective Taylor-Aris model (dashed line) on a moving mesh. The concentration profiles are given at times  $t = 100, 211$  and  $350$  seconds. The mesh deformation amplitude is  $a = \Delta y/3$ .

5.1.3. *Infinite adsorption in a fixed semi-infinite channel.* In this example we consider the steady flow of dissolved solutes coupled with infinite adsorption rate on the walls of the semi-infinite channel  $\mathbb{R}_+ \times (-H, H)$ . This is a unique problem that arises in reactive transport with strong sorption on the wall [25, 60]. In the bulk fluid, the solute dynamics are described by equation (43). However on the wall we need to note that the adsorption rate is unbounded, that is  $\hat{k}^* = +\infty$ . This requires a slightly different formulation of the flux equations on the active wall  $\Gamma_+$ . This equation is given by

$$(53) \quad -D^* \partial_{y^*} c^* = K_e \frac{\partial c^*}{\partial t^*}, \text{ on } |y^*| = H, x^* \in \mathbb{R}_+, t^* \in [0, T^*],$$

where  $K_e$  is the equilibrium adsorption constant as in the previous examples [25].

The study here, as in the previous cases, is to show that the FCT scheme is designed correctly for different reactive transport problems. So, we will consider the full 2D model discretized by the FEM-FCT on the fixed mesh, and on the moving mesh, and compare the solutions against the solution obtained from the 1D effective model, which we state next.

To do this first recall the characteristic variables we have stated in section 5.1.1. The only difference with the problem in this sub-section is that we now have a new characteristic time scale. The time scales  $T_A$ , and  $T_{DE}$  are rendered invalid as  $\hat{k}^* = \infty$ . Therefore, we introduce  $T_C = \frac{K_e B}{\varepsilon Q_R}$  which is a superficial chemical reaction time scale[25, 60]. Moreover, we choose  $T_R \approx T_L \approx T_C$ . The result is the following non-dimensional problem in the two dimensional fixed domain  $\Omega^+ = \mathbb{R}_+ \times (0, 1)$ :

$$\begin{cases} \frac{\partial c^\varepsilon}{\partial t} + Q(1-y^2) \frac{\partial c^\varepsilon}{\partial x} = D\varepsilon^\alpha \frac{\partial^2 c^\varepsilon}{\partial x^2} + D\varepsilon^{\alpha-2} \frac{\partial^2 c^\varepsilon}{\partial y^2}, & \text{in } \Omega^+ \times (0, T), \\ -D\varepsilon^{\alpha-2} \frac{\partial c^\varepsilon}{\partial y} = \frac{T_C}{T_L} K \frac{\partial c^\varepsilon}{\partial t}, & \text{on } \Sigma^+ \times (0, T) \\ c^\varepsilon(x, y, 0) = 1, & \text{for } \Omega^+ \\ c^\varepsilon(0, y, t) = 0, & \text{for } (y, t) \in (0, 1) \times (0, T) \\ \frac{\partial c^\varepsilon}{\partial y}(x, 0, t) = 0, & \text{for } (x, t) \in (0, +\infty) \times (0, T). \end{cases}$$

For the domain aspect ratio  $\varepsilon \ll 1$ , the following effective model, obtained through anisotropic singular perturbation expansion was derived in [48, 60]:

$$\begin{aligned} \left(1 + \frac{KT_C}{T_L}\right) \frac{\partial c_K}{\partial t} + \frac{2Q}{3} \frac{\partial c_K}{\partial x} &= \varepsilon^\alpha \tilde{D} \frac{\partial^2 c_K}{\partial x^2}, \\ \text{where } \tilde{D} &= D + \frac{8}{945} \frac{Q^2}{D} \varepsilon^{2(1-\alpha)} + \frac{4Q^2}{135D} \frac{T_C}{T_L} \frac{K(2+7KT_C/T_L)}{(1+KT_C/T_L)^2} \varepsilon^{2(1-\alpha)}. \end{aligned}$$

Here,  $K$  is the non-dimensional Damköhler number. In dimensional form, this model reads:

$$(54) \quad (1 + Da_K) \frac{\partial c_K^*}{\partial t^*} + \frac{2Q^*}{3} \frac{\partial c_K^*}{\partial x^*} = D^* \left(1 + \frac{4}{135} Pe_T^2 \left[\frac{2}{7} + \frac{Da_K(2+7Da_K)}{(1+Da_K)^2}\right]\right) \frac{\partial^2 c_K^*}{\partial (x^*)^2},$$

where  $Da_K = K_e/H$  is the transversal Damköhler number, and  $Pe_T = Q^*H/D^*$  is the transversal Péclet number. This effective model has an explicit solution obtained by the Laplace transform:

$$(55) \quad \begin{aligned} c_K^*(x^*, t^*) &= 1 - \frac{1}{\sqrt{\pi}} \left[ \int_{\frac{x^* - \sigma t^*}{2\sqrt{\beta t^*}}}^{+\infty} e^{-\eta^2} d\eta + e^{\frac{x^* \sigma}{\beta}} \int_{\frac{x^* + \sigma t^*}{2\sqrt{\beta t^*}}}^{+\infty} e^{-\eta^2} d\eta \right] \\ &= 1 - \frac{1}{2} \left[ \operatorname{erfc}\left(\frac{x - \sigma t^*}{2\sqrt{\beta t^*}}\right) + e^{\frac{x^* \sigma}{\beta}} \operatorname{erfc}\left(\frac{x + \sigma t^*}{2\sqrt{\beta t^*}}\right) \right]. \end{aligned}$$

The qualitative analysis of this result is presented in [48], where the non-dimensional effective concentration  $c_K$  is compared to the full non-dimensional concentration  $c^\varepsilon$ . We will use this result to verify our numerical simulation of the full  $2D$ , infinite wall adsorption problem in the next paragraph.

Our main interest is to compare the numerical results from the FCT scheme to those of the effective model based on the data in Table 3. More precisely, we compare the analytical solution to the average of the  $2D$  solution  $\langle c_K^* \rangle = \frac{1}{H} \int_0^H c^*(x^*, z, t^*) dz$ . We run a long simulation which corresponds to physical time of  $T^* = 5755$  seconds. Particular attention is given to the test times  $t^* = 863, 2877$ , and  $5755$  seconds. Note that  $t^* = 5755$  seconds corresponds to the characteristic time for the whole transport process, corresponding to the stipulated characteristic length. The computational domain  $\Omega = (0, L) \times (0, H)$  has  $L = 10$  meters. The uniform mesh has  $\Delta x^* = L/800$  and  $\Delta y^* = H/40$  meters, and the time step is  $\Delta t^* = 0.125$  seconds. From this we see that the CFL number is  $\nu = Q^* \Delta t / \Delta x = 3 \times 10^{-2}$ . The mesh Péclet number in this case is  $Pe_h = \frac{Q^* \Delta x}{D^*} = 187.5$ .

We also investigate the effect of the mesh movement. The mesh movement is not expected to have a significant effect on the numerical solution by the geometric conservation law. We thus compare the full  $2D$  numerical solution obtained using the ALE-FCT scheme, with amplitude for mesh deformation given by  $a = \frac{\Delta y}{3}$ .

**Table 3.** Parameter values in the case of an infinite adsorption rate  $\hat{k}^* = +\infty$  in a semi-infinite channel with fixed meshes.

Parameters	Values
Width of the slit: $H$	$5 \times 10^{-3}$ m
Characteristic length: $L_R$	0.8632 m
$\varepsilon = H/L_R$	$5.7924001 \times 10^{-3}$
Characteristic velocity: $Q^*$	$3 \times 10^{-3}$ m/s
Molecular diffusion: $D^*$	$2 \times 10^{-7}$ mol/m <sup>2</sup> s
Longitudinal Péclet number: $Pe = L_R Q^*/D^*$	$1.2948 \times 10^5$
$\alpha = \log Pe / \log(1/\varepsilon)$	1.83815052
Transversal Péclet number: $Pe_T = H Q^*/D^*$	75
Transversal Damköhler number: $Da_K = K_e/H$	1

The results for the fixed and moving mesh comparison to the analytical solution are given in Figure 10. Clearly, there is good agreement between the numerical and effective model solutions. The asymptotic error of the effective model is of order  $O(\varepsilon^{2(2-\alpha)})$ , as before, which amounts to approximately 0.1887 error, for the data used in this simulation. This means that the pointwise error should be less than or equal to this number. Indeed, if we sample 100 points at  $t = 5755$  seconds, we get that the maximum and minimum pointwise errors are given respectively by 0.055886 and  $-0.020591$  for the moving mesh case, and for the fixed mesh case they are given by 0.0481 and  $-0.0319$ . The upper bound is less than 0.056 for the moving mesh, and 0.05 for the fixed mesh, clearly well below the asymptotic error.

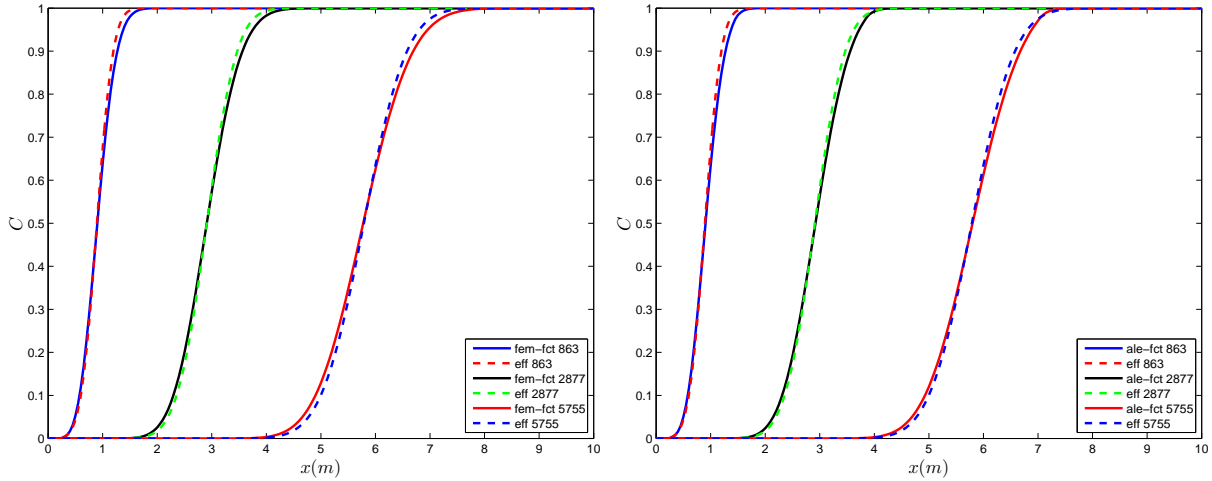


**Figure 10. Infinite adsorption; fixed channel, fixed (left) and moving (right) meshes.** Left: Comparison between the cross-sectional average of a solution obtained using the full FCT scheme (solid line) and the effective Taylor-Aris model (dashed line) on a fixed mesh. Right: Comparisons between the cross-sectional average of a solution obtained using the ALE-FCT scheme (solid line) and the effective Taylor-Aris model (dashed line) on a moving mesh. The concentration profiles are given at times  $t = 863, 2877$  and  $5755$  seconds. The mesh deformation amplitude is  $a = \Delta y/3$ .

5.1.4. *Nonlinear adsorption in a fixed semi-infinite channel.* In this example the adsorption isotherm under study is a nonlinear function  $\Lambda$ , as shown in equation (44). This means that we have the following boundary condition on the adsorbing wall:

$$-D^* \partial_y c^* = \partial_{t^*} \hat{c} = k_d (\Lambda(c^*) - \hat{c}), \text{ for, } |y^*| = H, x^* \in \mathbb{R}_+, t^* \in (0, T^*).$$

For this experiment, we choose the Langmuir isotherm, which is common in various solute transport problems such as chromatography and groundwater contaminant transport [35]. This isotherm is given by

$$\Lambda(c^*) = \frac{k_1^* c^*}{1 + k_2^* c^*}.$$

In the Langmuir isotherm, we have the desorption rate given by  $k_2^* = k_1^* = K_e$ , where  $K_e$  is as in the previous sections.

To state the effective model, derived in [60], we consider the following characteristic variables: the desorption rate is given by  $k_1 = k_1^*/k_{1R}$ , where  $k_{1R}$  is the characteristic size of the desorption rate; the second parameter  $k_2^*$  similarly has  $k_2 = k_2^*/k_{2R}$  as its non-dimensional counterpart. The remaining mass transfer parameters are treated as in the linear adsorption-desorption case, studied in sections 5.1.1 and 5.1.2. In addition to what has been considered, we introduce the timescale  $T_A = \frac{\hat{c}_R}{c_R k_{1R}}$ , which is the characteristic adsorption time, and  $T_{react} = H/k_{1R}$ , which is the superficial chemical reaction time scale for the nonlinear Langmuir isotherm. Moreover, we will have that  $T_L \approx T_A \approx \frac{1}{k_d^*}$ , and  $k_1$  and  $k_2$  are of order 1. The effective model for transport in  $(0, \infty) \times (-H, H) \times (0, T^*)$ , derived in [60], is given by:

$$\left\{ \begin{array}{l} \partial_{t^*} \left( c_N^* + \frac{\hat{c}_N}{H} \right) + \frac{\partial}{\partial x^*} \left( \frac{2Q^*}{3} c_N^* + \frac{Pe_T}{15} \Lambda(c_N^*) \right) \\ = D^* \left( 1 + \frac{8}{945} Pe_T^2 \right) \frac{\partial^2 c_N^*}{\partial (x^*)^2} + \frac{2k_d^* Pe_T}{45} \partial_{x^*} \hat{c}_N, \quad (x^*, t^*) \in \mathbb{R}_+ \times (0, T^*), \\ \partial_{t^*} \hat{c}_N = \Lambda(c_N^* + Pe_T \bar{c}_N^1) - k_d^* \hat{c}_N, \quad (x^*, t^*) \in \mathbb{R}_+ \times (0, T^*), \\ \bar{c}_N^1 = \frac{2H}{45} \partial_{x^*} c_N^* - \frac{1}{3} \partial_{t^*} \hat{c}_N, \quad (x^*, t^*) \in \mathbb{R}_+ \times (0, T^*), \\ c_N^*|_{x^*=0} = 1, \quad c_N^*|_{t^*=0} = 0, \quad \hat{c}_N|_{t^*=0} = 0. \end{array} \right.$$

We perform simulations with the data in Table 4, and with the adsorption rate  $k_d k_1^* = 0.190 \times 10^{-4}$  and  $k_2^* = K_e = H$ . We simulate this problem on the domain of length  $L = 2L_R$ , with  $\Delta x^* = L/150$ ,  $\Delta y^* = H/30$  and  $\Delta t^* = 0.1$ .

**Table 4.** Data for nonlinear adsorption-desorption in a semi-infinite slit

Parameters	Values
Width $H$	$5 \times 10^{-3}$ m
Characteristic length $L_R$	0.632 m
$\varepsilon = H/L_R$	$7.9113 \times 10^{-3}$
Characteristic velocity $Q^*$	$3 \times 10^{-3}$ m/s
Diffusion coefficient $D^*$	$2 \times 10^{-7}$ m <sup>2</sup> /s
Longitudinal Péclet number $Pe = L_R Q^*/D^*$	$9.48 \times 10^3$
$\alpha = \log(Pe)/\log(1/\varepsilon)$	1.8921440
Transversal Péclet number $Pe_T = H Q^*/D^*$	75

The results for this simulation are given in Figure 11. For both the FCT scheme and the ALE-FCT (with moving meshes), we have good agreement between the full 2D numerical solution and the 1D effective model. The pointwise error at the end of the simulation ( $T^* = 100$  seconds) falls within the interval  $[6.4172 \times 10^{-17}, 0.0386]$  for the fixed mesh, and in  $[-5 \times 10^{-5}, 0.0384]$  for the moving mesh, which indicates excellent agreement.

**5.2. Grid convergence for fixed and moving meshes.** In this section we study the grid convergence of the solution for both fixed and moving meshes. This will be done by comparing the difference between solutions defined on coarse meshes, and the solution defined on a fine mesh, called the reference solution. Moreover, we will also consider the mesh movement error. The examples we consider are the irreversible

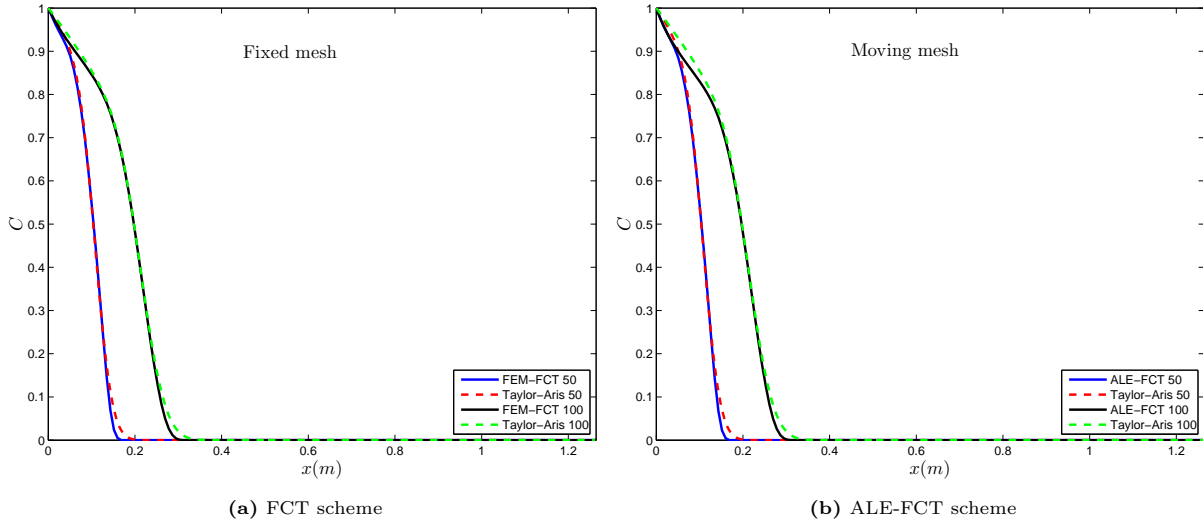


**Figure 11. Nonlinear Langmuir adsorption; fixed channel, fixed mesh (left) and moving mesh (right).** Left: Comparison between the cross-sectional average of a solution obtained using the full FCT scheme (solid line) and the effective Taylor-Aris model (dashed line) on a fixed mesh. Right: Comparisons between the cross-sectional average of a solution obtained using the ALE-FCT scheme (solid line) and the effective Taylor-Aris model (dashed line) on a moving mesh. The concentration profiles are given at times  $t = 50$  and  $100$  seconds. The mesh deformation amplitude is  $a = \Delta y/9$ .

transport problem, and the reversible transport problem. We compare the numerical solution to the reference solution utilizing error expressions given as follows

$$(56) \quad E_1(h) = \sum_i m_i |c_i - c_{ref}(x_i, y_i)| \approx \|c_h - c^{ref}\|_{L^1},$$

$$(57) \quad E_2(h) = \sqrt{\sum_i m_i |c_i - c_{ref}(x_i, y_i)|^2} \approx \|c_h - c^{ref}\|_{L^2}.$$

These formulae for error computation will be applied to a sequence of nested grids.  $E_1(h)$  will denote the error on the coarser mesh, and  $E_1(h/2)$  is the error on the refined mesh. The order of convergence  $p$  is given by

$$p = \log_2 \left[ \frac{E_2(h)}{E_2(h/2)} \right].$$

The relative error is defined as

$$(58) \quad E_1^{rel}(h) = \frac{E_1(h)}{\sum_i m_i |c_{ref}(x_i, y_i)|} \approx \frac{\|c_h - c^{ref}\|_{L^1}}{\|c^{ref}\|_{L^1}},$$

$$(59) \quad E_2^{rel}(h) = \frac{E_2(h)}{\sqrt{\sum_i m_i |c_{ref}(x_i, y_i)|^2}} \approx \frac{\|c_h - c^{ref}\|_{L^2}}{\|c^{ref}\|_{L^2}}.$$

We consider the **linear adsorption-desorption reaction**, and **nonlinear Langmuir** transport. The reference solution is the standard Galerkin solution calculated at the finest mesh.

**5.2.1. Linear adsorption-desorption reactive transport.** We consider the adsorption-desorption problem as computed in section 5.1.2. As in the reversible case, the coarsest mesh has  $\Delta x = L/200$ ,  $\Delta y = H/10$  and

$\Delta t = 0.01$ . We refine by halving mesh sizes, and the finest mesh is attained at  $(\frac{\Delta x}{8}, \frac{\Delta y}{8}, \frac{\Delta t}{8})$ . Table 5 shows the results obtained for the fixed mesh, while Table 6 shows the results for the moving mesh.

$\Delta t$	$\Delta x$	$E_2(h)$	$E_1(h)$	$E_2^{rel}(h)(\%)$	$E_1^{rel}(h)(\%)$	$\ c_h - c^{ref}\ _{L^\infty}$
0.01	$L/200$	0.0013	$4.3709 \times 10^{-5}$	4.7162	4.6851	0.0950
0.005	$L/400$	$6.8863 \times 10^{-4}$	$2.2475 \times 10^{-5}$	2.5200	2.4090	0.0508
0.0025	$L/800$	$3.5237 \times 10^{-4}$	$1.1292 \times 10^{-5}$	1.2895	1.2104	0.0261

**Table 5.** Space and time grid convergence for adsorption-desorption at constant CFL number for the FCT fixed mesh scheme at  $t = 50$  seconds, the end of the simulation

$\Delta t$	$\Delta x$	$E_2(h)$	$E_1(h)$	$E_2^{rel}(h)(\%)$	$E_1^{rel}(h)(\%)$	$\ c_h - c^{ref}\ _{L^\infty}$
0.01	$L/200$	0.0027	$8.9016 \times 10^{-5}$	11.5122	11.9333	0.1563
0.005	$L/400$	0.0012	$3.8037 \times 10^{-5}$	4.9846	5.0992	0.1074
0.0025	$L/800$	$4.8922 \times 10^{-4}$	$1.5825 \times 10^{-5}$	2.0930	2.1215	0.0682

**Table 6.** Space and time grid convergence for adsorption-desorption at constant CFL number for the ALE-FCT moving mesh scheme at  $t = 50$  seconds, the end of the simulation

Let  $p_1 = \log_2(E_2(\Delta x)/E_2(\Delta x/2))$ , and let  $p_2 = \log_2(E_2(\Delta x/2)/E_2(\Delta x/4))$  denote the orders of accuracy on the coarser and finer meshes respectively. Then, effective order of accuracy for the FCT scheme is given by  $p_1 = 0.9178$  on the coarser meshes, and  $p_2 = 0.9656$  on the finer meshes. The effective order of accuracy for the ALE-FCT scheme is given by  $p_1 = 1.1699$  on the coarser meshes, and  $p_2 = 1.2945$ , on the finer meshes. Moreover, Table 7 shows the  $L^2$  errors between the moving mesh solution and the reference fixed mesh solution on the finest mesh.

$\Delta x$	$\Delta t$	$\frac{\ c_{moving-fixed}\ _{L^2}}{\ c_{fixed}\ _{L^2}} (\%)$	$\frac{\ c_{moving-fixed}\ _{L^1}}{\ c_{fixed}\ _{L^1}} (\%)$
0.01	$L/200$	11.5662	11.9923
0.005	$L/400$	5.0353	5.1567
0.0025	$L/800$	2.1430	2.1786

**Table 7.** At  $t = 50$  seconds, the moving mesh error  $\frac{\|c_{moving-fixed}\|_{L^*}}{\|c_{fixed}\|_{L^*}}$  values for space and time grid convergence with constant CFL number

5.2.2. *Nonlinear Langmuir adsorption reactive transport.* We consider the nonlinear Langmuir adsorption problem as computed in section 5.1.4. The data used in this case is similar to the linear reversible problem with  $k_d \hat{k}_1^* = 0.190 \times 10^{-4}$  and  $\hat{k}_2^* = K_e = H$ . The coarsest mesh has  $\Delta x = L/50$ ,  $\Delta y = H/10$  and  $\Delta t = 0.01$ . We refine by halving mesh sizes and the finest mesh is attained at  $(\frac{\Delta x}{8}, \frac{\Delta y}{8}, \frac{\Delta t}{8})$ . Table 8 shows the results obtained for the fixed mesh, while Table 9 shows the results for the moving mesh.

$\Delta t$	$\Delta x$	$E_2(h)$	$E_1(h)$	$E_2^{rel}(h)(\%)$	$E_1^{rel}(h)(\%)$	$\ c_h - c^{ref}\ _{L^\infty}$
0.05	$L/50$	0.0012	$5.5056 \times 10^{-5}$	3.2915	3.1096	0.0437
0.025	$L/100$	$6.0652 \times 10^{-4}$	$2.6985 \times 10^{-5}$	1.6233	1.5241	0.0289
0.0175	$L/200$	$2.6450 \times 10^{-4}$	$1.1829 \times 10^{-5}$	0.7079	0.6681	0.0127

**Table 8.** Space and time grid convergence for nonlinear adsorption at constant CFL number for the FCT fixed mesh scheme at  $t = 100$  seconds, the end of the simulation

Let  $p_1$ , and let  $p_2$  denote the orders of accuracy on the coarser and finer meshes respectively as in the previous section. Then, effective order of accuracy for the FCT scheme is given by  $p_1 = 0.9844$  on the coarser meshes, and  $p_2 = 0.9542$  on the finer meshes. The effective order of accuracy for the ALE-FCT scheme is given by  $p_1 = 1.1973$  on the coarser meshes, and  $p_2 = 1.0388$ , on the finer meshes. Moreover, Table 10 shows the  $L^2$  errors between the moving mesh solution and the reference fixed mesh solution on the finest mesh.

$\Delta t$	$\Delta x$	$E_2(h)$	$E_1(h)$	$E_2^{rel}(h)(\%)$	$E_1^{rel}(h)(\%)$	$\ c_h - c^{ref}\ _{L^\infty}$
0.05	$L/50$	0.0031	$3.7288 \times 10^{-4}$	3.1029	2.9489	0.0587
0.025	$L/100$	0.0016	$1.9812 \times 10^{-4}$	1.6015	1.5668	0.0422
0.0175	$L/200$	$7.7879 \times 10^{-4}$	$9.6313 \times 10^{-5}$	0.7877	0.7617	0.0276

**Table 9.** Space and time grid convergence for nonlinear adsorption at constant CFL number for the ALE-FCT moving mesh scheme at  $t = 100$  seconds, the end of the simulation

$\Delta x$	$\Delta t$	$\frac{\ c_{moving-cfixed}\ _{L^2}}{\ c_{fixed}\ _{L^2}} (\%)$	$\frac{\ c_{moving-cfixed}\ _{L^1}}{\ c_{fixed}\ _{L^1}} (\%)$
0.05	$L/50$	3.0990	2.7836
0.025	$L/100$	1.8861	1.7680
0.0175	$L/200$	1.6435	1.4481

**Table 10.** At  $t = 100$  seconds, the moving mesh error  $\frac{\|c_{moving-cfixed}\|_{L^*}}{\|c_{fixed}\|_{L^*}}$  values for space and time grid convergence with constant CFL number

**5.3. Linear and nonlinear reactive transport in moving domains.** We consider reactive transport in a micro-channel which is compliant and defined by  $\Omega(t) = (0, L) \times (0, H + \eta(x, t))$ , where  $H = 0.15 \text{ mm}$ , and  $L > 0$  large. The boundary deformation is defined by the following top boundary function

$$\eta(x, t) = a \cos(2\pi x) \sin(2\pi t), \text{ with, } a = H/20.$$

We study targeted adsorption-desorption on the moving micro-channel wall in which a catalyst material on the wall draws solute molecules to it by a heterogeneous chemical process at the upper part of the domain. The heterogeneous process is either the linear Henry's law, or the nonlinear non-equilibrium Langmuir isotherm. For this process, one component solute species are modelled using the convection-diffusion equation defined on the moving domain  $\Omega(t)$ , as given by equation (1). The flow of the fluid is described by the numerical solution to the Navier-Stokes equation in moving domains, previously calculated using a solver developed in [33]. See problem (2).

For an initial condition of the bulk solute, we consider a tracer slug in the fluid. This slug, resembling a controlled injection of solute into the flow, is convected by the flow of the above viscous fluid of density  $\rho = 10^{-3} \text{ g/mm}^3$  and viscosity  $\nu = 1 \text{ g/mm s}$ . The calculations are performed with the no slip boundary condition on the deforming top boundary ( $v_1 = 0$ , and  $v_2 = \partial_t \eta$ ), and the no-slip condition at the fixed bottom boundary ( $\mathbf{v} = \mathbf{0}$ ). The flow is driven by a pressure gradient  $\bar{p}$  through the normal stress  $\boldsymbol{\sigma} \mathbf{n} = -\bar{p} \mathbf{n}$ . The pressure gradient is approximately  $250 \text{ g/mm}^2 \text{ s}^2$ , resulting in longitudinal velocity ranging between  $[-4.23 \times 10^{-3}, 1.45 \times 10^{-1}]$ , and the transversal velocity ranging between  $[0.0, 0.777626]$  for a convection dominated flow regime.

We will also consider the mass transfer actions under different values of the diffusion coefficient  $D$  in  $\text{mm}^2/\text{s}$ . We will consider the values  $D = 1.0 \times 10^{-3}$  and  $1.0 \times 10^{-2}$ . As part of the simulation, we will monitor how increases in chemical diffusivity affects the targeted adsorption process.

The reaction rate constants for the heterogeneous process considered here are from experimental adsorption of acetone from a water solution to a carbon adsorbent on the wall [58]. We also vary adsorption constants to monitor the performance of the scheme in response to given values  $k_a = 0.190, 0.760$  all in  $\text{mm}/\text{s}$ . We keep the equilibrium adsorption-desorption rate the same at  $K_e = 0.146$ , so the desorption constant also has to change to give the values  $k_d = 1.3014, 5.2055$  also in  $\text{mm}/\text{s}$ .

The effects of chemistry on the transport process are effectively characterized by the values of the transversal and longitudinal Damköhler numbers  $Da_T$  and  $Da_L$ , respectively. The longitudinal Damköhler number is given by  $Da_L := \frac{L_R k_a}{\langle v \rangle}$ , the transversal Damköhler number is given by  $Da_T = k_a H / D$ . The mesh Damköhler number is given by  $Da_h = h k_a / \langle v \rangle$ , where  $\langle v \rangle$  is the average velocity in the channel, or characteristic velocity in the timescale of the chemical reaction. The effects of dispersion on the transport process are characterized by the values of the Péclet number. The longitudinal Péclet number and transversal Péclet number are defined respectively by  $Pe_L = \langle v \rangle L / D$  and  $Pe_T = H \langle v \rangle / D$ .

The data for convection dominated flow in a deformable microchannel is given in Table 11. From the data in Table 11, we get that the longitudinal and transversal Péclet numbers are given respectively by  $Pe_L = 311.1, 3.11 \times 10^3$  and  $Pe_T = 5.832, 58.32$ , corresponding to  $D = 1 \times 10^{-2}, 1 \times 10^{-3}$ . The longitudinal Damköhler number has values  $Da_L = 3.909, 15.6373$  corresponding to  $k_a = 0.190$  and  $0.760$ . The transversal Damköhler number is given by  $2.850$ , when  $k_a = 0.190$ , and the diffusion coefficient is given by  $D = 1 \times 10^{-2}$ .

$L$ (mm)	Length of reference domain	8
$H$ (mm)	Height of reference domain	0.15
$T$ (s)	Total time of simulation	10.0
$\Delta P$ (g/mm <sup>2</sup> s <sup>2</sup> )	Pressure drop	250
$\langle v \rangle$ (mm/s)	Average longitudinal velocity	$3.888 \times 10^{-1}$
$\Delta t, \Delta x, \Delta y$	Mesh dimensions	0.005

**Table 11.** The parameters with step sizes on the reference mesh. The  $x$  direction is kept the same, while the mesh nodes move vertically due to wall movements, and the velocity is  $\mathbf{v} = (v_1, v_2)$ .

5.3.1. *Mass conservation in the moving domain.* Let  $M_f(t) = \int_0^L \int_0^{H+\eta(x,t)} c_h^f(x, y, t) dy dx$  and  $M_w(t) = \int_0^L c_h^w(x, t) dx$  to be the bulk solute mass and wall solute mass respectively. The sum  $M(t) = M_f(t) + M_w(t)$  is the total mass of the chemical species involved in the process. We plot the results for both linear and nonlinear isotherm simulation in Figure 12. The variation of the adsorption rate  $k_a$  and the variation of the diffusivity of the solute  $D$  do not affect the total mass, showing the resilience of the scheme. Indeed for all the different cases,  $M(t)$  does not change in a short 10 second simulation where we do not have the species reaching the end of the computational domain.

5.3.2. *Outlet solution average in the moving domain.* The next test is the study of concentration values the end of the deformable channel. In chromatography models, this corresponds to the detector position where solute peaks show separation when many species are involved [35]. In this case we have only one species in a narrow column affected by the flow of the fluid carrying the species under study. For both linear and nonlinear isotherms we observe the profile typical to those observed in elution experiments and models. The first two plots in Figure 13 correspond to  $D = 1 \times 10^{-3}$  show very little difference for both linear and nonlinear isotherms even with great variation in  $k_a$  which is  $0.190$  on the left and  $0.760$  on the right. Increase in the diffusion coefficient to  $D = 1 \times 10^{-2}$  results in large solute quantities reaching the compliant wall which is shown in the last two plots of Figure 13. The difference between the linear and nonlinear cases here show the need to choose carefully which isotherm to use with increase in species concentration.

5.3.3. *Wall solute concentration in the moving domain.* It is also essential to carefully consider the wall solute concentration values for positivity and response to varying parameters such as diffusion and reaction. Figure 14 shows the wall solute concentration  $c_h^w$  at varying times in the simulation. The linear and nonlinear cases show significant differences on how much chemical is adsorbed. The difference between the linear isotherm and nonlinear isotherm is magnified with increase in diffusion coefficient  $D$  from  $1 \times 10^{-3}$  to  $1 \times 10^{-2}$ . Notice that the wall solute concentration is consistently non-negative for all the values of  $D$  and  $k_a$  considered.

5.3.4. *Full 2D moving domain profiles.* The next study considers full 2-dimensional snapshots of the simulation at different times for a simulation of 5 seconds for both linear and nonlinear problems. We show the full bulk fluid concentration  $c^f$  profiles where  $D = 1 \times 10^{-3}$  and  $k_a = 0.190$ . The linear problem solution is shown in Figure 15, and the nonlinear problem solution in Figure 16. The snapshots are taken at times  $t = 0, 0.6, 1.1, 1.6$  seconds. In these snapshots, the solution maintains the property of non-negativity, and the solution is always below 1. The color scheme has been set to range from 0 to 0.1 to capture more vividly the concentration profile at later times where much dispersion has occurred. While the linear and nonlinear cases show similar concentration profiles within the fluid, it will be shown in the next section that the concentration at the wall is significantly influenced by the type of isotherm (linear v.s. nonlinear) chosen to model the wall adsorption.

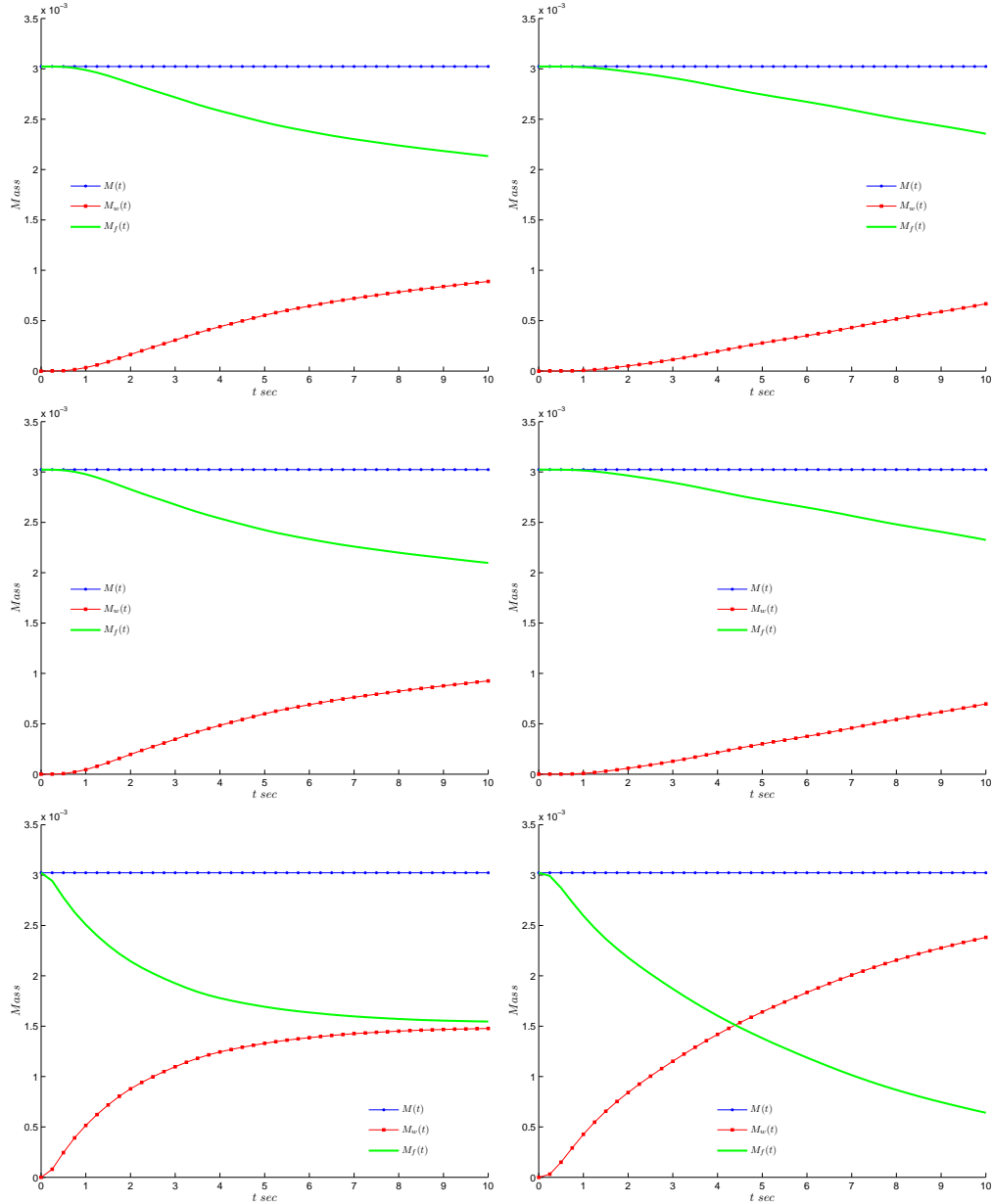


**Figure 12.** The total mass  $M(t) = M_f(t) + M_w(t)$  for the linear and nonlinear isotherms. The first two figures are for diffusion coefficient  $D = 1 \times 10^{-3}$  and reaction rate  $k_a = 0.190$  for linear (left) and nonlinear (right) isotherms. For the middle two figures (left and right) we have the same diffusivity, but the reaction rate is given by  $k_a = 0.760$ . The last two figures are for the same reactions rates, but with  $D = 1 \times 10^{-2}$ . Notice that in this case we have at a point in time more mass on the wall than in the bulk fluid. The total mass is conserved in all cases.

**5.3.5. Fixed vs moving wall adsorption.** We now consider a comparison of the wall solute concentration  $c^w(x, t)$  between a fixed and a moving channel wall. We compare  $c^w$  on  $\hat{\Sigma} = \{(x, y) \mid x \in (0, L), y = H\}$ , to  $c^w$  on  $\Sigma(t)$ . In a controlled separation of various solutes, it is often essential to change the physical apparatus to enhance the separation. In this case, it is of interest to see if a controlled movement of the adsorbing wall can enhance uptake of the solute on the wall. In this process, the quantity  $c^f$  is converted to  $c^w$  by the flux equation (1)<sub>2</sub>. This is also relevant in medical applications, for example, in adsorption of nano-particles carrying cancer drugs by the vasculature. One of the open questions is whether enhanced adsorption of

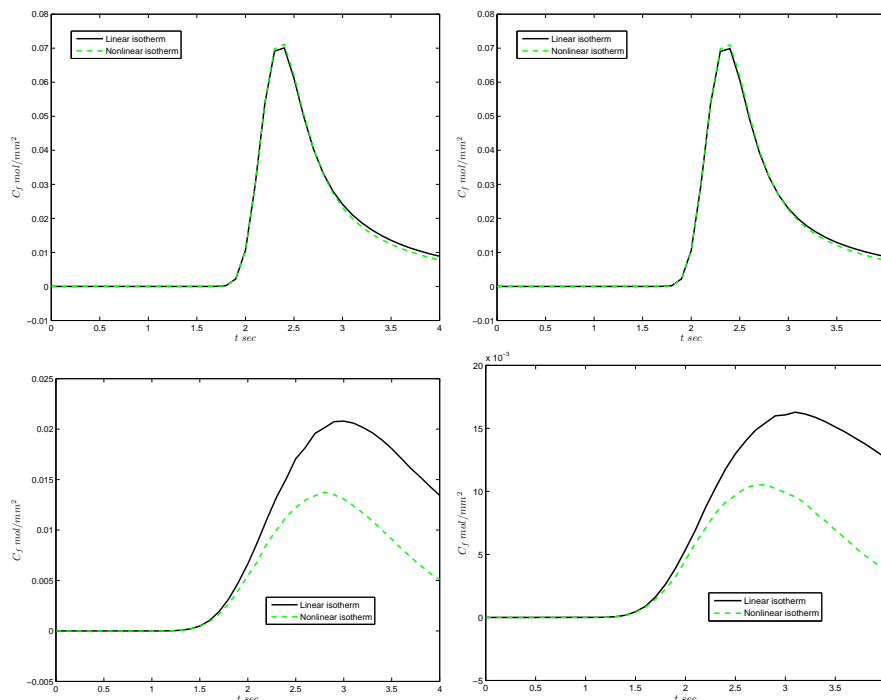


**Figure 13.** The chromatogram for the single solute species at the outlet. In time progression we observe the peak for the solute. The first two figures are for diffusion coefficient  $D = 1 \times 10^{-3}$  and reaction rates  $k_a = 0.190$  and  $k_d = 0.760$ . The last two figures are for the same reactions rates with  $D = 1 \times 10^{-2}$ . The difference in the second row of pictures show the nonlinear isotherm sensitivity when high concentration quickly reaches the adsorbing wall.

cancer drugs can be achieved by exciting the cancerous tissue with ultrasound. Our results presented in this section show that this is, indeed, the case.

We simulate reactive transport for  $t = 5$  seconds, with diffusion coefficient  $D = 1 \times 10^{-3}$ , and adsorption rate  $k_a = 0.3812$ . We start with  $c^w(x, 0) = 0$ , for all  $x \in (0, L)$ . In both the linear and nonlinear cases, the moving wall case shows enhanced adsorption to the solid wall from the bulk fluid. The snapshots of this are shown in Figures 17 and 18. We also observe that the adsorption occurs when the dissolved solutes reach the wall by dispersion. Figure 19 shows a comparison between the fixed and moving wall simulations with nonlinear Langmuir isotherm. The left panels correspond to the fixed channel case, while the right panels correspond to the channel with the moving wall. A significant increase in wall adsorption due to the motion of the channel wall can be observed.

## 6. CONCLUSION

In this paper we considered a model for reactive solute transport in deformable media undergoing general non-equilibrium adsorption-desorption processes on the moving solid surface. We developed a novel Patankar-based linearization technique, which ensures mass-conservative time discretization. Furthermore, the classical FCT scheme was extended to the ALE-FCT scheme for reactive transport models in moving domains. The scheme was shown to be mass conservative and positivity preserving. The positivity was ensured under a CFL type constrain on  $\Delta t$ .

Several numerical experiments were presented. First, problems on fixed domains were considered for linear adsorption-desorption, irreversible reactions, infinite adsorption and nonlinear Langmuir kinetics. To verify the correct implementation of the scheme for the moving domain case, both fixed and moving meshes were considered first on the **fixed** domain, and the solutions on both the fixed and moving meshes were shown to be in good agreement. In all the cases our (averaged) 2D solutions were compared with the known 1D solutions

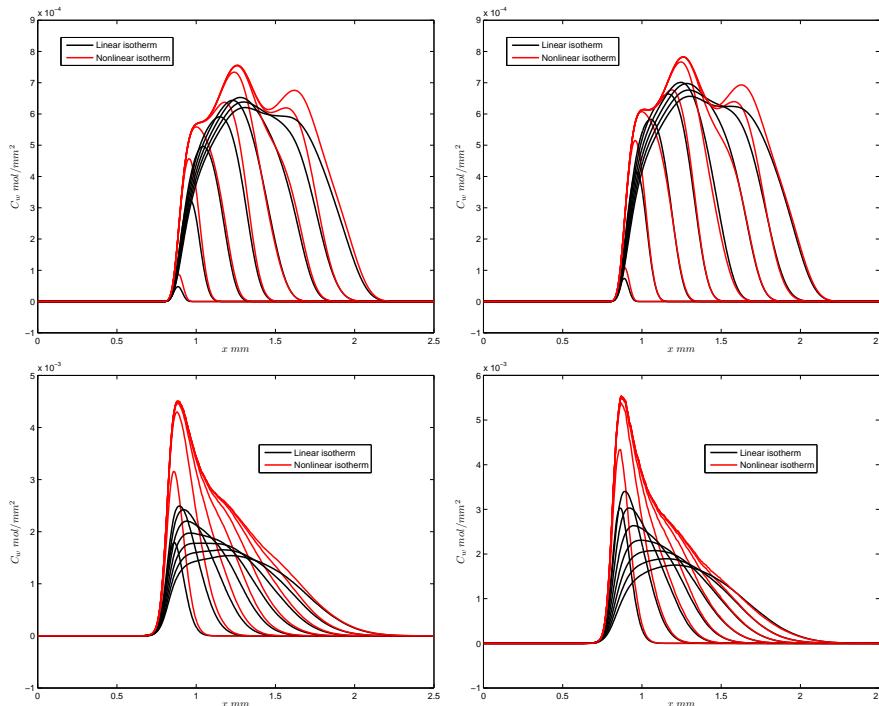


**Figure 14.** The linear Henry’s law and nonlinear Langmuir wall concentration  $c_w$  at varying times. The first two figures are for diffusion  $D = 1 \times 10^{-3}$  and the bottom two figures for the diffusion  $D = 1 \times 10^{-2}$ . In the first two there is not much difference in the amount of solute adsorbed on the wall. In the second case with high diffusion, the difference is enhanced by the amount of solute reaching the wall.

of the corresponding reduced models, showing excellent comparison. Our scheme showed to perform better than the standard FEM scheme on both fixed and moving meshes, producing no oscillations around steep concentration fronts, which were visible with a standard FEM scheme. Finally, we considered the nonlinear Langmuir adsorption and tested our scheme based on Patankar linearization. Again, the numerical results obtained using the FCT scheme were in excellent agreement with those from established effective models on fixed domains.

We studied next the grid convergence of the numerical solution to a reference solution on a fine mesh. We observed that the FEM-FCT scheme and the ALE-FCT scheme were both first order accurate when we refined the mesh in both space and time (keeping the CFL number constant). This shows the expected 1-st order behavior of FCT schemes. We also studied the error resulting from mesh motion. We saw that for both linear adsorption, and for nonlinear Langmuir adsorption, the  $L^2$  relative error decreased with mesh refinement to only 2% after second halving of the mesh size.

The last study concerned deformable channels with thin elastic, chemically active walls. For both linear and nonlinear adsorption, the ALE-FCT scheme was mass conservative, and positivity preserving. Next we compared the influence of linear and nonlinear isotherms. We observed that when very small amounts of the solute reach the wall, the linear and nonlinear isotherms behave in the same way, as expected. If we increase diffusion, there is big difference in the wall concentration between the linear and nonlinear isotherm cases. Lastly, we compared the wall adsorption between a fixed and moving compliant channel. We observed that the moving channel wall enhances the solute uptake as the wall solute concentration was shown to be larger on the moving wall than on the fixed wall throughout the simulation. This is an important piece of information relevant for many applications, including cancer drug delivery using nano particles. Our results indicate that periodic excitation of the cancerous tissue using e.g., ultrasound, would enhance drug uptake by the vascular walls into the cancerous tissue, paving a way for new methodologies in cancer drug delivery.

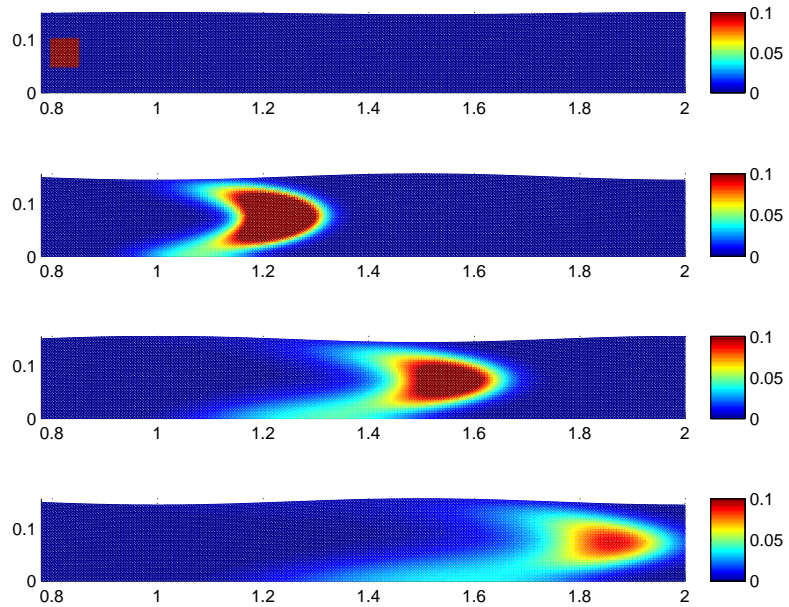


**Figure 15.** Advection-diffusion of a solute (Taylor dispersion regime) with **linear adsorption-desorption** at the top wall of a channel of length 2, at 4 different times. The initial condition is shown by the first figure. The top wall of the channel is moving in a sinusoidal fashion. The values of concentration are between 0 and 1. The legend shows compressed colors around red for concentration values between 0.1 and 1.

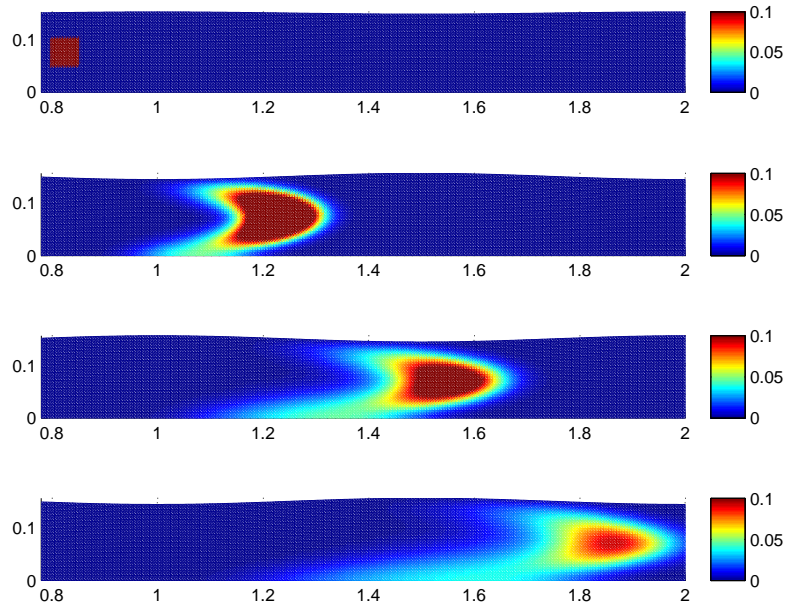


**Figure 16.** Advection-diffusion of a solute (Taylor dispersion regime) with **nonlinear adsorption** at the top wall of a channel of length 2, at 4 different times. The initial condition is shown by the first figure. The top wall of the channel is moving in a sinusoidal fashion. The values of concentration are between 0 and 1. The legend shows compressed colors around red for concentration values between 0.1 and 1.

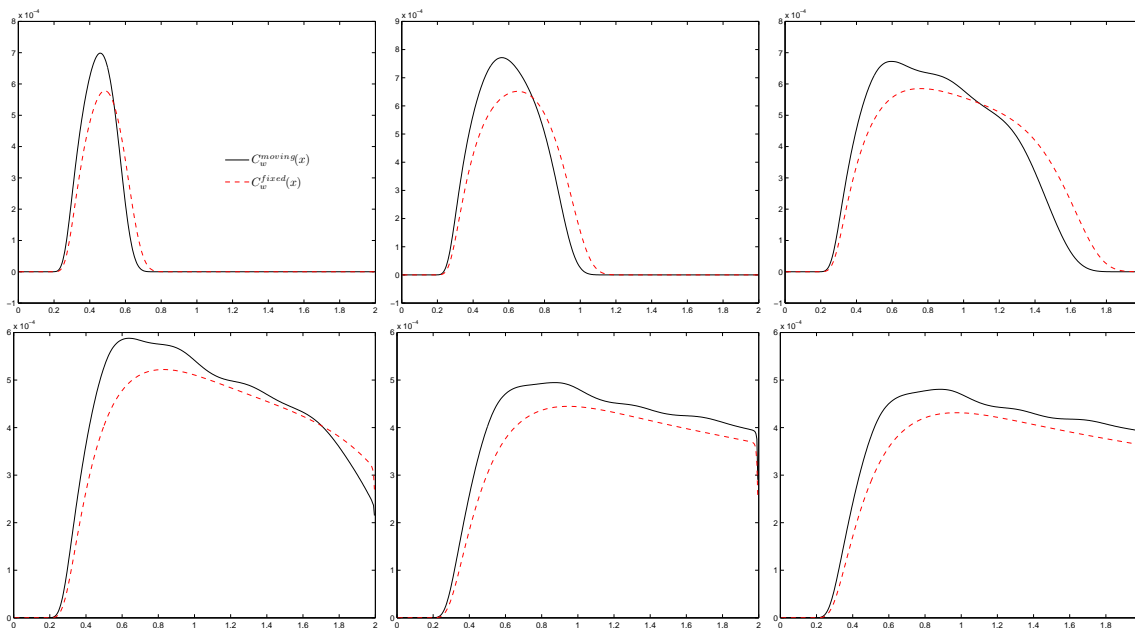


**Figure 17.** The comparison between fixed and moving channel simulation for transport characterised by the linear Henry's law. These are  $c_w$  versus  $x$  snapshots for the fixed and moving domain at times  $t = 0.7, 1.2, 2.2, 3.2, 4.7, 5.0$  seconds.

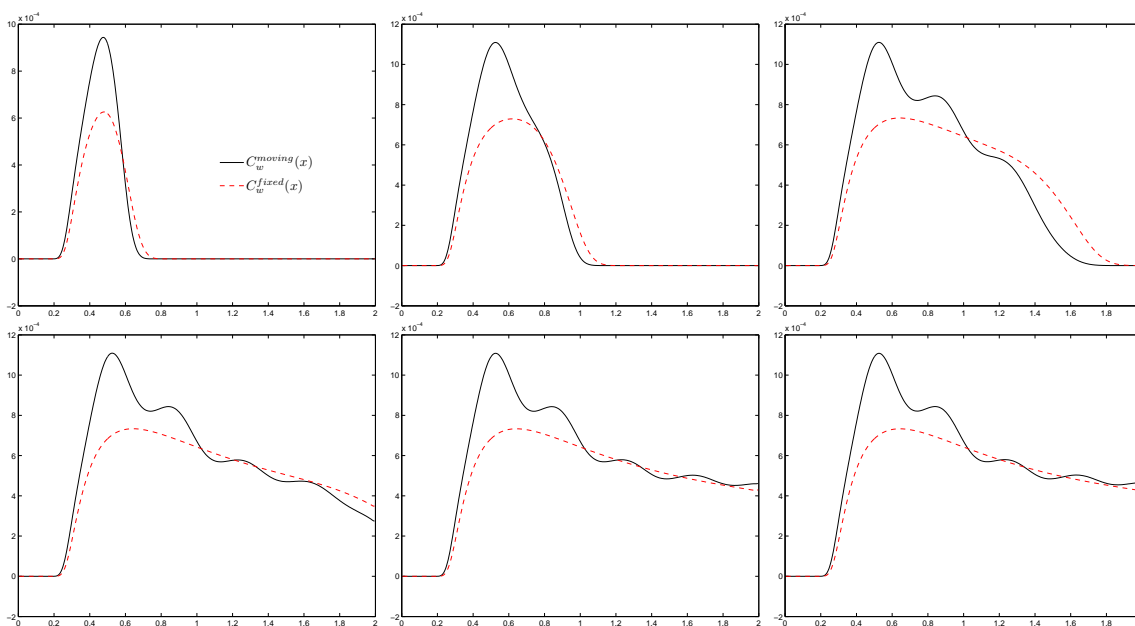


**Figure 18.** The comparison between fixed and moving channel simulation for transport characterised by the nonlinear Langmuir isotherm. These are  $c_w$  versus  $x$  snapshots for the fixed and moving domain at times  $t = 0.7, 1.2, 2.2, 3.2, 4.7, 5.0$  seconds.

#### ACKNOWLEDGEMENTS

The authors thank the anonymous reviewer whose comments and suggestions have greatly improved the manuscript.

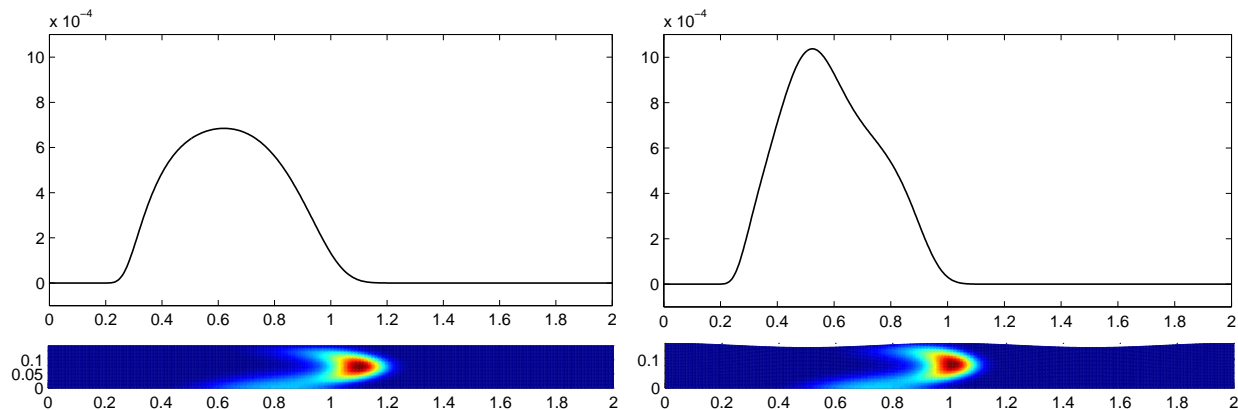


**Figure 19.** Comparison between the fixed wall (left) and moving wall (right) simulations at  $t = 1.2$  seconds for nonlinear Langmuir adsorption. The top figures show the plots of  $c^w$  versus  $x$ , and the bottom figures show the full  $c^f$  profile in  $\Omega$  (left), and  $\Omega(t)$  (right).

### REFERENCES

- [1] G. Allaire, R. Brizzi, A. Mikelić, and A. Piatnitski, *Two-scale expansion with drift approach to the Taylor dispersion for reactive transport through porous media*, Chemical Engineering Science **65** (2010), 2292-2300.
- [2] G. Allaire, A. Mikelić, and A. Piatnitski, *Homogenization approach to the dispersion theory for reactive transport through porous media*, SIAM Journal of Mathematical Analysis **42** (2010), no. 1, 125-144.
- [3] R. Aris, Proceedings of the Royal Society, London A **1956** (1956), no. 1200, 67-77.
- [4] ———, *Vectors, Tensors and the Basic Equations of Fluid Mechanics*, Dover Publications, 1990.
- [5] P. Atkins and J. de Paula, *Atkin's Physical Chemistry*, 8th ed., W. H. Freeman, 2006.
- [6] S. Badia and R. Codina, *Analysis of a stabilized finite element approximation of the transient convection-diffusion using and ALE framework*, SIAM Journal of Numerical Analysis **44** (2006), no. 5, 2159-2197.
- [7] S. Badia, F. Nobile, and C. Vergara, *Fluid-structure partitioned procedures based on Robin transmission conditions*, J. Comput. Phys. **227** (2008), 7027-7051.
- [8] V. Balakotaiah and H. Chang, *Dispersion of Chemical Solutes in Chromatographs and Reactors*, Phil. Trans. R. Soc. Lond. A **351** (1995), no. 1695, 39-75.
- [9] J. Barrett and P. Knabner, *Finite element approximation of the transport of reactive solutes in porous media. Part I: Error estimates for nonequilibrium adsorption processes*, SIAM Journal of Numerical Analysis **34** (1997), no. 1, 201-227.
- [10] R. Bird, W. Stewart, and E. Lightfoot, *Transport Phenomena*, 2nd ed., John Wiley & Sons, Inc, 2006.
- [11] O. Boiarkine, D. Kuzmin, S. Čanić, G. Guidoboni, and A. Mikelić, *A positivity-preserving ALE finite element scheme for convection-diffusion equations in moving domains*, Journal of Computational Physics **230** (2011), 2896-2914.
- [12] D. Bolster, M. Dentz, and T. Le Borgne, *Solute dispersion in channels with periodically varying apertures*, Physics of Fluids **21** (2009), 056601.
- [13] J.P. Boris and D. L. Book, *Flux-corrected transport. I. SHASTA, A fluid transport algorithm that works*, Journal of Computational Physics **11** (1973), 38-69.
- [14] M. Bukač, S. Čanić, R. Glowinski, B. Muha, and A. Quaini, *A Modular, Operator Splitting Scheme for Fluid-Structure Interaction Problems with Thick Structure*, International Journal of Numerical Methods in Fluids **29** (2013), 1192-1213.
- [15] M. Bukač and S. Čanić, *Longitudinal displacement in viscoelastic arteries: a novel fluid-structure interaction computational model and experimental validation.*, Mathematical Biosciences and Engineering **10** (2013), no. 2, 295-318.
- [16] H. Burchard, E. Deleersnijder, and A. Meister, *A high-order conservative Patankar-type discretization for stiff systems of production-destruction equations*, Applied Numerical Mathematics **47** (2003), 1-30.
- [17] H. Burchard, E. Deleersnijder, and A. Meister, *Application of modified Patankar schemes to stiff biogeochemical models for the water column*, Ocean Dynamics **55** (2005), 326-337.
- [18] H. Burchard, K. Bolding, W. Kühn, A. Meister, T. Neumann, and L. Umlauf, *Description of a flexible and extendable physical-biogeochemical model system for the water column*, Journal of Marine Systems **61** (2006), 180-211.
- [19] Sunčica Čanić, Andro Mikelić, Tae-Beom Kim, and Giovanna Guidoboni, *Existence of a Unique Solution to a Nonlinear Moving-Boundary Problem of Mixed Type Arising in Modeling Blood Flow* (Alberto and Chen Bressan Gui-Qiang G. and Lewicka, ed.), The IMA Volumes in Mathematics and its Applications, vol. 153, Springer US, 2011 (English).
- [20] S. Čanić and B. Muha, *Existence of a Weak Solution to a Nonlinear Fluid-Structure Interaction Problem Modeling the Flow of an Incompressible, Viscous Fluid in a Cylinder with Deformable Walls*, Archive for Rational Mechanics and Analysis **207** (2013), 919-968.
- [21] ———, *A nonlinear moving boundary problem of parabolic-hyperbolic-hyperbolic fluid -multi-layered structure interaction problems*, Americal Institute of Mathematical Sciences (AIMS) Publications (2013).

- [22] S. Čanić, B. Muha, and M. Bukač, *Fluid-structure interaction in biomedical applications book chapter: Fluid-structure interaction with multiple structural layers: theory and numerics.*, Advances in fluid mechanics (2013).
- [23] S. Čanić and B. Muha, *Existence of a solution to a fluid-multi-layered structure interaction problem*, Journal of Differential Equations **256** (2014), 658-706.
- [24] S. Chakraborty and V. Balakotaiah, *Low-dimensional models for describing mixing effects in laminar flow tubular reactors*, Chemical Engineering Science **57** (2002), 2545-2564.
- [25] C. Choquet and A. Mikelić, *Laplace transform approach to the rigorous upscaling of the infinite adsorption rate reactive flow under dominant Peclet number through a pore*, Applicable Analysis **87** (2008), 1373-1395.
- [26] ———, *Rigorous upscaling of the reactive flow with finite kinetics and under dominant Péclet number*, Continuum Mechanics and Thermodynamics **21** (2009), 125-140.
- [27] C. Choquet and C. Rosier, *Effective models for reactive flow under a dominant Péclet number and order one Damköhler number: Numerical simulations*, Nonlinear Analysis: Real World Applications **15** (2012), 345-360.
- [28] C.A.J. Fletcher, *The group finite element formulation*, Computer Methods in Applied Mechanics and Engineering **37** (1983), 225-244.
- [29] L. Formaggia and F. Nobile, *A stability analysis for the arbitrary Lagrangian Eulerian formulation with finite elements*, East-West Journal of Numerical Mathematics **7** (1999), no. 2, 105-131.
- [30] L. Formaggia and F. Nobile, *Stability analysis of second-order time accurate schemes for ALE-FEM*, Computer methods in applied mechanics and engineering **193** (2004), 4097-4116.
- [31] L. Formaggia, S. Minisini, and P. Zunino, *Modeling polymeric controlled drug release and transport phenomena in the arterial tissue*, Mathematical Models and Methods in Applied Sciences **20** (2010), no. 10, 1759-1786.
- [32] L. Formaggia and A. Scotti, *Positivity and conservation properties of some integration schemes for mass action kinetics*, SIAM Journal of Numerical Analysis **49** (2011), no. 3, 1267-1288.
- [33] G. Guidoboni, R. Glowinski, N. Cavallini, and S. Čanić, *Stable loosely-coupled-type algorithm for fluid-structure interaction in blood flow*, Journal of Computational Physics **228** (2009), 6916-6937.
- [34] S. B. Gogoi, *Adsorption-Desorption of Surfactant for Enhanced Oil Recovery*, Transport in Porous Media **90** (2011), 589-604.
- [35] G. Guiochon, S. Shirazi, and A. Katti, *Fundamentals of preparative and nonlinear chromatography*, 2nd ed., Academic Press, 2006.
- [36] V. John and E. Schmeier, *Finite element methods for time-dependent convection-diffusion-reaction equations with small diffusion*, Comput. Methods Appl. Mech. Engrg. **198** (2008), 475-494.
- [37] T. Kim, S. Čanić, and G. Guidoboni, *Existence and uniqueness of a solution to a three-dimensional axially symmetric biot problem arising in modeling blood flow*, Communications on Pure and Applied Analysis **9** (2010), 839-865.
- [38] K. Kumar, M. Wheeler, and T. Wick, *Reactive flow and reaction-induced boundary movement in a thin channel*, SIAM Journal of Scientific Computing **35**, no. 6, B1235-B1266.
- [39] K. Kumar, T. Noorden, and I. Pop, *Upscaling of reactive flows in domains with moving oscillating boundaries*, Discrete and Continuous Dynamical Systems Series S **7** (2014), no. 1.
- [40] D. Kuzmin and M. Möller, *Algebraic flux correction. I. Scalar conservation laws. Flux-corrected transport* (R. Löhner and S. Turek D. Kuzmin, ed.), Scientific Computation, Springer Berlin Heidelberg, 2005.
- [41] D. Kuzmin, *Explicit and implicit FEM-FCT algorithms with flux linearization*, Journal of Computational Physics **228** (2009), 2517-2534.
- [42] ———, *Linearity-preserving flux correction and convergence acceleration for constrained Galerkin scheme*, Journal of Computational and Applied Mathematics **236** (2012), 2317-2337.
- [43] H. Langtangen, *Computational Partial Differential Equations, Numerical Methods and Diffpack Programming, Vol I*, 2nd ed., Texts in Computational Science and Engineering, Springer-Verlag, 2003.
- [44] R. Löhner, K. Morgan, J. Peraire, and M. Vahdati, *Finite element flux-corrected transport (FEM-FCT) for the Euler and Navier-Stokes equations*, Int. J. Numer. Meth. Fluids **7** (1987), 1093-1109.
- [45] R. Löhner, K. Morgan, M. Vahdati, J.P. Boris, and D.L. Book, *FEM-FCT: combining unstructured grids with high resolution*, Commun. Appl. Numer. Methods **4** (1988), 717-729.
- [46] R. MacKinnon and G. Carey, *Positivity-preserving, flux-limited finite-difference and finite-element methods for reactive transport*, International Journal for Numerical Methods **41** (2003), 151-183.
- [47] A. Mikelić, V. Devigne, and C.J. van Duijn, *Rigorous upscaling of the reactive flow through a pore, under dominant Péclet and Damköhler numbers*, SIAM Journal of Mathematical Analysis **38** (2006), no. 4, 1262-1287.
- [48] A. Mikelić and C. Rosier, *Rigorous upscaling of the infinite adsorption rate reactive flow under dominant Péclet number through a pore*, Annali dell'Università di Ferrara **53** (2007), 333-359.
- [49] A. Mikelić and C.J. van Duijn, *Rigorous derivation of a hyperbolic model for Taylor dispersion*, Math Models Methods Appl. Sci. **21** (2011), 1095.
- [50] M. Möller, D. Kuzmin, and D. Kourounis, *Implicit FEM-FCT algorithms and discrete Newton methods for transient convection problems*, International Journal of Numerical Methods in Fluids **57** (2008), 761-792.
- [51] C. Ng, *Dispersion in steady and oscillatory flows through a tube with reversible and irreversible wall reactions*, Proceedings of the Royal Society A **462** (2006), no. 2066, 481-515.
- [52] F. Nobile, *Numerical approximation of fluid-structure interaction problems with applications to haemodynamics*, École polytechnique fédérale de Lausanne, 2001.

- [53] E. Marušić-Paloka and I. Pažanin, *On reactive solute transport through a curved pipe*, Applied Mathematics Letters **24** (2011), 878-882.
- [54] V. Prigiobbe, M. A.Hesse, and S. L. Bryant, *Anomalous Reactive Transport in the Framework of the Theory of Chromatography*, Transport in Porous Media **93** (2012), 127-145.
- [55] F. Radu and I. Pop, *Newton method for reactive solute transport with equilibrium sorption in porous media*, Journal of Computational and Applied Mathematics **234** (2010), 2118-2127.
- [56] J. Rubinstein and R. Mauri, *Dispersion and Convection in Periodic Porous Media*, SIAM Journal on Applied Mathematics **46** (1986), no. 6, 1018-1023.
- [57] G. Scovazzi and A. López Ortega, *Algebraic flux correction and geometric conservation in ALE computations*, 2nd ed. (R. Löhner and S. Turek D. Kuzmin, ed.), Springer: Scientific Computation, Springer, 2012 (English).
- [58] J.D. Seadler and E.J. Henley, *Separation Process Principles*, 2nd ed., John Wiley & Sons Inc., 2005.
- [59] G. Taylor, *Dispersion of Soluble Matter in Solvent Flowing Slowly through a Tube*, Proceedings of the Royal Society of London. Series A, Mathematical and Physical Sciences **219** (1953), no. 1137, 186-203.
- [60] C.J. van Duijn, A. Mikelić, I.S. Pop, and C. Rosier, *Effective Dispersion Equations for Reactive Flows with Dominant Péclet and Damköhler Numbers*, Vol. 34, 2008.
- [61] D. Wolf, *Kinetics of Heterogeneous Catalytic Reactions*, Springer Series in Chemical Physics, vol. 75, 2004.
- [62] S.T. Zalesak, *Fully multidimensional flux-corrected transport algorithms for fluids*, Journal of Computational Physics **31** (1979), 335-362.
- [63] P. Zunino, *Mathematical and numerical modeling of mass transfer in the vascular system*, École polytechnique fédérale de Lausanne, 2002.